

## White Dwarf Merger Remnants with Cooling Delays on the Q Branch Lack Strong Magnetism

LOU BAYA OULD ROUIS ,<sup>1</sup> J. J. HERMES ,<sup>1</sup> JOSEPH A. GUIDRY ,<sup>1,\*</sup> SIHAO CHENG (程思浩) ,<sup>2</sup> MUKREMIN KILIC ,<sup>3</sup> OLIVIER VINCENT ,<sup>4</sup> PIERRE BERGERON ,<sup>4</sup> SIMON BLOUIN ,<sup>5</sup> ADAM MOSS ,<sup>6</sup> ISAAC D. LOPEZ ,<sup>7</sup> AND GRACYN JEWETT 

<sup>1</sup>Department of Astronomy & Institute for Astrophysical Research Boston University Boston, MA 02215, USA

<sup>2</sup>Institute for Advanced Study, 1 Einstein Dr., Princeton, NJ 08540, USA

<sup>3</sup>Homer L. Dodge Department of Physics and Astronomy, University of Oklahoma, 440 W. Brooks St., Norman, OK 73019, USA

<sup>4</sup>Département de Physique, Université de Montréal, C.P. 6128, Succ. Centre-Ville, Montréal, Québec, Canada

<sup>5</sup>Department of Physics and Astronomy, University of Victoria, Victoria, BC V8W 2Y2, Canada

<sup>6</sup>Department of Astronomy, University of Florida, 211 Bryant Space Science Center, Gainesville, FL 32611, USA

<sup>7</sup>Department of Physics and Astronomy, Iowa State University, Ames, IA 50011, USA

(Received December 3, 2025; Revised January 23, 2026; Accepted February 2, 2026)

Submitted to ApJ

### ABSTRACT

A population of anomalous ultra-massive white dwarfs discovered with Gaia, often referred to as the Q branch, show high (multi-Gyr) cooling delays produced by exotic physical mechanisms. They are believed to be the products of stellar mergers, but the exact origin and formation channel remain unclear. We obtained a spectroscopically complete, volume-limited sample of the Q branch region within 100 pc, and found significant differences in atmospheric composition and rotation rates as a function of tangential velocity. In particular, we discover that stellar remnants with the longest cooling delays do not show strong magnetism nor detectable short-period rotational variability, as opposed to what is generally believed for double-degenerate mergers. This indicates that either these white dwarfs arise from a formation channel with no strong magnetism induced, or that the magnetism produced from the merger dissipates over the cooling delay timescales. Our follow-up photometry has also discovered pulsations in the second and third hydrogen-dominated DAQ white dwarfs, one hotter than 15,500 K, possibly extending the boundaries of the DAV instability strip for white dwarfs with thin hydrogen layers.

**Keywords:** White dwarf stars 1799 — Stellar astronomy 1583 — Atmospheric composition 2120 — Stellar mergers 2157 — Magnetic fields 994 — Stellar evolution 1599

### 1. INTRODUCTION

The Q branch refers to an over-density of ultra-massive white dwarfs ( $M_{\text{WD}} > 1.08 M_{\odot}$ ) on the color-magnitude diagram lining up with the carbon/oxygen-core (C/O) white dwarf crystallization sequence (Tremblay et al. 2019). It was first discovered from Gaia, which revolutionized our understanding of white dwarf

cooling evolution thanks to large datasets of white dwarfs (Gaia Collaboration et al. 2018; Gentile Fusillo et al. 2019, 2021). Using the precise proper motions and distance measurements provided by Gaia, Cheng et al. (2019) provided the first detailed study of the Q branch region by breaking the sample up by their kinematics, finding that roughly 6% of white dwarfs passing through the Q branch will encounter cooling delays of at least 6 Gyr that cannot only be explained by the latent heat release from crystallization or by merger delay times.

Following years of efforts to understand this cooling delay phenomenon (Camisassa et al. 2019; Blouin et al. 2020a,b; Bauer et al. 2020; Caplan et al. 2020, 2021;

Corresponding author: Lou Baya Ould Rouis  
 lbor@bu.edu

\* NSF Graduate Research Fellow

Camisassa et al. 2021; Wu et al. 2022; Fleury et al. 2022, 2023), the Q branch cooling anomaly is likely best explained as a byproduct of the distillation of neutron-rich species like  $^{22}\text{Ne}$  (Blouin et al. 2020a, 2021; Bédard et al. 2024). An excess of  $^{22}\text{Ne}$  allows for a phase separation process that creates buoyant crystals which then float up, displacing  $^{22}\text{Ne}$ -rich liquid down. This process liberates gravitational energy and pauses the white dwarf cooling for timescales greater than predicted by theoretical cooling evolution (Blouin et al. 2021).

The required amount of neon for this cooling delay mechanism greatly exceeds solar abundances, several times higher than  $X_{^{22}\text{Ne}} \simeq 0.016$  (Shen et al. 2023). Exactly how such objects get produced is still poorly understood, though a fraction of white dwarfs with multi-Gyr cooling delays could result from single-star evolution with high initial metallicities ( $X_{^{22}\text{Ne}} > 0.025$ ) (Bariantos et al. 2025). Merger scenarios of helium white dwarf engulfment by main-sequence or red giant stars can result in roughly  $0.7\text{ M}_\odot$  C/O-core white dwarfs with  $^{22}\text{Ne}$  abundances high enough to distill  $^{22}\text{Ne}$  (Rui & Fuller 2025).

Considering the progenitor scenario is crucial for confirming the physics behind the Q branch. Broadly, understanding the precise evolutionary history of white dwarfs is essential to accurately determine total ages, and keep using white dwarfs as cosmic clocks for cosmochronology (e.g., Fontaine et al. 2001; Pathak et al. 2025). Stellar mergers of any type complicate cosmochronology.

Roughly 50% of massive white dwarfs ( $M_{\text{WD}} > 0.9\text{ M}_\odot$ ) are expected to be merger remnants (Toonen et al. 2012; Cheng et al. 2020; Kilic et al. 2023). Specifically, of all merger types, double-degenerate (WD+WD) mergers are responsible for about half of massive isolated white dwarfs (Temmink et al. 2020). These remnants are best characterized by strong magnetism from an induced dynamo during the merger (e.g., García-Berro et al. 2012), rapid overall rotation from the conserved angular momentum accelerated at short orbital distances in compact binaries (e.g., Schwab 2021), and fast kinematics typical of older populations from dynamical motions around the Galaxy (e.g., Holmberg et al. 2009). White dwarfs may also arise from binary mergers at other phases, from the main-sequence to the red-giant phases.

White dwarf stars with masses greater than roughly  $1.05\text{ M}_\odot$  originating from single-star evolution are expected to have oxygen-neon cores (O/Ne) rather than C/O cores (Siess 2007; Lauffer et al. 2018). Yet, the pile up of white dwarfs in the Q branch region ( $M_{\text{WD}} > 1.08\text{ M}_\odot$ ) aligns with the C/O crystallization

onset branch (Tremblay et al. 2019), which starts later than the onset of crystallization in O/Ne-core white dwarfs. Additionally, the physical process of  $^{22}\text{Ne}$  distillation requires C/O-core white dwarfs to produce the strength of cooling delays actually observed in the region (Bédard et al. 2024). Thus, the population of white dwarfs on the Q branch with high cooling delays likely harbor C/O cores. In order to be ultra-massive with a C/O core, the object needs to have been produced through a merger that avoided carbon ignition (Dan et al. 2014). The location and shape of the Q branch can only be reproduced by including white dwarfs with very thin helium layers, which is also inconsistent with a single star evolution scenario (Bédard et al. 2024).

Thus, white dwarfs in the Q branch region with high cooling delays should be ultra-massive merger remnants with C/O cores and super-solar metallicities. Shen et al. (2023) suggest that such objects can be produced by the merger of a C/O-core white dwarf with the He-rich core of a subgiant star, and that the occurrence of this type of merger could explain most if not all of the observed delays on the Q branch. In this scenario, the initial C/O-core white dwarf and subgiant star do not require abnormal initial metallicities. Rather, the merger produces an extra amount of  $^{14}\text{N}$  that gets burned into  $^{26}\text{Mg}$  and leads to the distillation process along with the extra  $^{22}\text{Ne}$  once crystallization begins. Still, models do not predict exactly how much hydrogen and carbon enrich the helium envelope of the remnant following the merger, which would affect the abundance of  $^{26}\text{Mg}$  produced, and therefore how long the cooling delays can be (Shen et al. 2023).

In this paper, we are interested in testing the formation pathways of white dwarfs with high cooling delays in the Q branch region in order to eventually inform the mechanisms responsible for the delays. With this 100-pc volume-limited study, we present evidence that ultra-massive white dwarfs with high cooling delays do not show strong magnetism, and make up a distinct population of merger remnants with thin hydrogen layers, weak magnetism, and slow rotation.

In Section 2, we detail the sample selection for the Q branch white dwarfs. In Section 3, we describe the spectroscopic observations. In Section 4, we present the spectral type distributions of kinematically selected subsets of white dwarfs in the Q branch region, describing the atmospheric compositions and magnetism of each sample, alongside a comparison sample of canonical-mass white dwarfs within the same temperature range. In Section 5.2, we investigate the photometric variability of white dwarfs in the Q branch region to constrain the fraction of rapid rotators and pulsators. In Section 6, we

discuss the merger history channels which cannot lead to the high cooling delays Q branch merger remnants, and propose plausible pathways.

## 2. SAMPLE SELECTION

The region of the color-magnitude diagram we refer to as the Q branch is selected as described in Cheng et al. (2019) from Gaia sources. We choose to limit this study to 100 pc in order to complete a spectroscopic sample.

The boundaries of the Q branch region are defined in Cheng et al. (2019), and were determined using Gaia DR2 parallaxes and magnitudes. If we update all parameters to the most recent Gaia data release (Gaia DR3, Gentile Fusillo et al. 2021), the boundaries are slightly shifted, and a dozen objects fall out of our sample boundaries, while eight new objects fall inside. For continuity with the observational work on the Q branch, we choose to use Gaia DR2 parameters. The overall sample size and statistics are not significantly affected by adopting the updated parameters.

Our sample of white dwarfs on the Q branch region within 100 pc contains 75 objects distributed across the entire sky, presented in Table C1. A color-magnitude diagram is presented in Figure 1.

### 2.1. Kinematics of the Q branch

Ultra-massive white dwarfs should have slow transverse velocities because they are young ( $\tau_{\text{total}} < 2 \text{ Gyr}$ ), based on age-velocity-relations (Holmberg et al. 2009). Abnormally high tangential velocities can be used as a proxy to identify merger products, as the age reset of merger events causes the remnant white dwarf to appear younger than its true total age. In the Q branch region, a population of white dwarfs with abnormally high kinematics indicates additional cooling delays, estimated to be at least 6 Gyr. Such delays cannot be explained only by a merger delay (Cheng et al. 2019).

To isolate the white dwarfs with high cooling delays, we divide the Q branch region into two subsets, a kinematically fast population ( $v_t > 50 \text{ km s}^{-1}$ ) that we refer to as the delayed subset and a kinematically slow population ( $v_t < 50 \text{ km s}^{-1}$ ) that we refer to as the young subset. Here,  $v_t$  is defined as:

$$v_t = 4.74 \frac{\sqrt{\mu_\alpha^2 + \mu_\delta^2}}{\varpi} \quad (1)$$

where  $\mu_\alpha$  and  $\mu_\delta$  are the proper motions in right ascension and declination, and  $\varpi$  is the parallax.

The delayed subset is composed of 30 white dwarfs with high cooling delays characterized by fast kinematics. The white dwarfs in the delayed subset are randomly distributed through the Q branch region and highlighted

in Figure 1. The young subset is composed of 45 white dwarfs with the expected velocity distribution of a population with total ages  $\tau_{\text{total}} < 2 \text{ Gyr}$ , in agreement with theoretical cooling models. The white dwarfs in the young subset are also randomly distributed through the Q branch region and represented by the unfilled circles in Figure 1.

We opt for a cutoff transverse velocity of  $v_t = 50 \text{ km s}^{-1}$  as identified in Wegg & Phinney (2012) to be a reliable signature of merger remnants. Additionally, the kinematics of the class of DAQ white dwarfs (hydrogen-dominated atmospheres with atomic carbon absorption lines) that have been associated with the Q branch cooling delay population (Kilic et al. 2024) reveal that out of the six published cases within 100 pc, Hollands et al. (2020); Kilic et al. (2024); Sahu et al. (2025), all but one have transverse velocity  $v_t > 51 \text{ km s}^{-1}$ . The exception, J0551+4135, discovered in Hollands et al. (2020), has a high radial velocity, bringing its total space velocity to  $129 \pm 5 \text{ km s}^{-1}$  (in the local standard of rest).

A conservative lower limit of  $v_t > 50 \text{ km s}^{-1}$  does not prevent other merger remnants with high radial velocity to contaminate the young Q branch subset, as we only consider transverse velocity in our work. Therefore, the young subset could include a fraction of O/Ne-core white dwarfs resulting from single-star evolution, along with a contamination of merger remnants: some without noteworthy cooling delays, some with high radial velocity but typical transverse velocity, as well as merger remnants possibly at the very beginning of their time stuck on the Q branch not exhibiting cooling delays just yet. Crucially, our kinematic cut ensures that the delayed subset only contains objects with high cooling delays in order to consider this population as independent.

We compare the simplified transverse velocity measurements ( $v_t$ ) with transverse velocity measurements in Galactic coordinates ( $v_l, v_b$ ) corrected for the motion of the Sun around the Milky Way. All 30 white dwarfs with  $v_t > 50 \text{ km s}^{-1}$ , have combined  $\sqrt{v_l^2 + v_b^2} > 40 \text{ km s}^{-1}$ , and 30 out of the 33 objects with combined  $\sqrt{v_l^2 + v_b^2} > 40 \text{ km s}^{-1}$  are included in the delayed subset. Choosing either of the two methods does not significantly alter our results, so we adopt  $v_t$  parameters for clarity. The transverse velocity values for all white dwarfs in the Q branch region within 100 pc are reported in Table C1.

### 2.2. Comparison Sample

We also analyze a sample of 94 canonical-mass white dwarfs within 100 pc to use as comparison. The comparison sample is composed of average mass white dwarfs

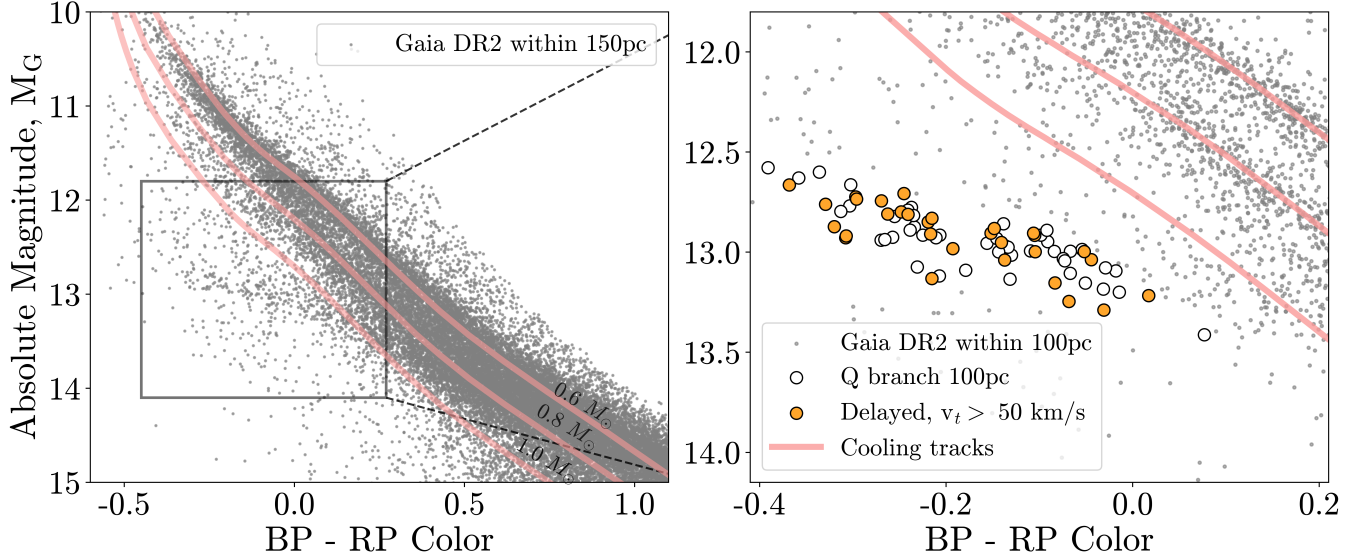


**Figure 1.** Color-magnitude diagram of the Gaia white dwarfs (gray points, Gentile Fusillo et al. 2019) within 150 pc (left) and 100 pc (right). The left panel highlights the over-density referred to as the Q branch. The right panel zooms in on the region to show our full sample of 75 white dwarfs in the Q branch region within 100pc as defined in (Cheng et al. 2019), where the targets filled in orange make the delayed subset with high cooling delay as indicated by their high kinematics ( $v_t > 50 \text{ km s}^{-1}$ ). White dwarfs of a given mass are expected to cool from the top left to the bottom right along theoretical cooling tracks shown here (solid pink lines) for  $0.6 M_\odot$ ,  $0.8 M_\odot$ , and  $1.0 M_\odot$  (Blouin et al. 2020a).

$(0.55 M_\odot < M_{\text{WD}} < 0.80 M_\odot)$  that we select to be in the same temperature range as the Q branch region within 100 pc assuming photometrically-derived atmospheric parameters with hydrogen-dominated models, or  $10,000 \text{ K} < T_{\text{eff}} < 26,000 \text{ K}$ . We limit the comparison sample to objects in Gaia DR3 with an SDSS spectrum available, and use the SDSS spectral type classifications and photometrically derived atmospheric parameters for H-rich objects from (Gentile Fusillo et al. 2021). To make sure that the comparative sample only includes white dwarfs compatible with single-star evolution, we limit the kinematics of this sample to the slow subset of the Q branch region, with transverse velocity  $v_t < 50 \text{ km s}^{-1}$ .

### 3. SPECTROSCOPIC OBSERVATIONS

We aim to compare the atmospheric compositions of the white dwarfs in each subset of the Q branch region described in Section 2.

Spectroscopy offers insight on the atmospheric composition of white dwarfs. The strong surface gravity creates stratified layers, where elements heavier than hydrogen or helium sink below the photosphere on timescales shorter than white dwarf cooling ages (e.g., Fontaine & Michaud 1979). With optical spectroscopy, we can identify absorption lines and infer spectral types based on the dominating element present in the atmosphere such as hydrogen (DA), helium (DB), carbon (DQ), or metals such as calcium (DZ) (e.g., Sion et al. 1983). When we

can identify more than one element in white dwarf spectra, the spectral type reflects the order of the dominating species. It is worth noting that from ground-based low resolution spectroscopy in the temperature range of our sample ( $T_{\text{eff}} > 10,000 \text{ K}$ ), we are limited in our detection of metals as those transitions become weaker with increasing temperature, so the relative absorption strength decreases (e.g., Zuckerman et al. 2003).

Spectroscopy also allows us to identify Zeeman splitting of spectral features, which is characteristic of strong magnetism, with typical sensitivity to fields of strength greater than 1 MG for low-resolution optical spectra (Moss et al. 2025).

We first query the literature for published spectra of our targets. We were able to recover spectra for 53 of the 75 sources in our sample with the Montreal White Dwarf Database (MWDD; Dufour et al. 2017) published in Croom et al. (2004); Gianninas et al. (2011); Guo et al. (2015); Kilic et al. (2020); O'Brien et al. (2023); Jewett et al. (2024), as well as archival SDSS spectra (Kleinman et al. 2013).

We conduct observing campaigns for the remaining 22 uncharacterized white dwarfs in the 100 pc Q branch region. We also follow up two targets discussed in the literature without public spectra available (Koester & Weidemann 1982; Croom et al. 2004), and two targets with published spectra but low signal-to-noise ratio in order to confirm their spectral types.

We include here all 26 new spectra we acquired. Of these, 22 were observed with the Goodman spectrograph on the 4.1-meter Southern Astrophysical Research (SOAR) Telescope with a resolution  $R \approx 2000$  (Clemens et al. 2004). Three targets were observed with the GMOS spectrograph on the 8.1-meter Gemini South telescope with a resolution  $R \approx 1500$  (Hook et al. 2004). The remaining new spectrum was obtained with the De-Veny spectrograph on the 4.3-meter Lowell Discovery Telescope (LDT) with a resolution  $R \approx 1500$  (Bida et al. 2014). All spectra were reduced and flux calibrated using `PypeIt` routines (Prochaska et al. 2020a,b). Table A1 details the dates, gratings and setups used for all 26 new observations. The new spectra are shown in Figures A.1, A.2, A.3, and A.4, sorted by spectral type.

#### 4. SPECTRAL TYPES OF Q BRANCH WHITE DWARFS

In the magnitude-limited spectroscopic sample of white dwarfs in the Q branch region analyzed by Cheng et al. (2019), roughly 50% of white dwarfs with high cooling delays were classified as DQs (i.e. showing atomic carbon in their atmospheres). From existing spectroscopy in the literature, the authors also noted that most massive DQs are concentrated on the Q branch. The other half of these high-cooling-delay white dwarfs were classified as hydrogen-dominated DA white dwarfs.

Figure 2 shows our main classification results, highlighting the atmospheric composition of three different populations, namely the delayed Q branch subset ( $v_t > 50 \text{ km s}^{-1}$ ; left panel), the young Q branch subset ( $v_t < 50 \text{ km s}^{-1}$ ; middle panel), and an SDSS average-mass white dwarf sample in the same temperature range for comparison (right panel). All fractional counts are reported in Table 1 for clarity.

##### 4.1. Delayed subset

Even with a larger sample than Cheng et al. (2019), we find the same result that 15 out of 30 white dwarfs (50%) in the delayed Q branch subset show carbon-dominated atmospheres. In most cases we also see hydrogen, characteristic of the DQA and DAQ spectral types (11/15).

The DAQ subclass is particularly noteworthy. DAQ white dwarfs are expected to have thin hydrogen layer diluted with a deeper carbon-rich semi-convective envelope. There have been a total of 16 published white dwarfs with this spectral type, including six DAQs within 100 pc, found in a relatively narrow parameter space (Hollands et al. 2020; Kilic et al. 2024; Jewett et al. 2024; Sahu et al. 2025). These white dwarfs are ultra-massive ( $0.98 \text{ M}_\odot < M_{\text{WD}} < 1.31 \text{ M}_\odot$ ), hot ( $13,000 \text{ K} <$

$T_{\text{eff}} < 23,000 \text{ K}$ ), and a large fraction (10/16) have high tangential velocities ( $v_t \geq 50 \text{ km s}^{-1}$ ). Here, we report a new DAQ white dwarf, WD J170145.15–524609.22 (shown in Figure A.2), bringing the class to seven published objects within 100 pc, and 17 published DAQs in total. The best-fitting DAQ model has  $\log \text{C/H} = 0.43$ ,  $T_{\text{eff}} = 19,104 \pm 330 \text{ K}$  and a mass of  $1.23 \pm 0.01 \text{ M}_\odot$ , using the photometric fitting method with DAQ model grids as detailed in Kilic et al. (2024) and the spectrum fit is presented in Figure A.5. This new DAQ becomes the hottest and most massive white dwarf of the class within 100 pc. All DAQ white dwarfs found to date are in the Q branch region (Kilic et al. 2024).

The remaining 15 out of the 30 delayed Q branch white dwarfs have hydrogen-dominated atmospheres (50%), with no other element visible from optical spectra. We note that the DAQ discovered in Sahu et al. (2025) (WD 0525+526 or WD J052950.25+523953.39) is reported as a DA in this study in order to compare the spectral type distribution of the Q branch within the same resolution and wavelength range, and because WD J052950.25+523953.39 does not show significant carbon absorption in optical spectroscopy. It is possible that other DAs in the delayed subset exhibit traces of carbon but require more sensitive UV spectra to detect those transitions. Thus, the overall atmospheric composition of the delayed subset is in agreement with the findings from Cheng et al. (2019).

We do not detect strong magnetism within a limit of 1 MG among any of the delayed Q branch white dwarfs within 100 pc (0/30). This suggests that <4.5% of delayed white dwarfs on the Q branch show strong magnetism. We investigate archival SDSS spectra for the delayed Q branch beyond 100 pc, and in this increased sample are able to identify some white dwarfs with strong magnetism, such as the DH WD J090632.65+080716.16 which is at a distance of 144 pc (Bailer-Jones et al. 2021). This reveals that strong magnetism in white dwarfs with high cooling delays is rare.

##### 4.2. Young subset

The young Q branch subset is dominated by hydrogen-rich (DA) white dwarfs. Of the 45 objects in this subset, we observe 25 DA white dwarfs (56%). Seven white dwarfs are carbon-dominated (18%), of which more than half also show hydrogen (4/7; spectral type DAQ/DQA).

We detect Zeeman splitting of hydrogen in three of the 45 young subset white dwarfs (7% DAH, all fields  $B > 2.8 \text{ MG}$ ). We estimate magnetic field strength based on Zeeman hydrogen splitting diagrams (or

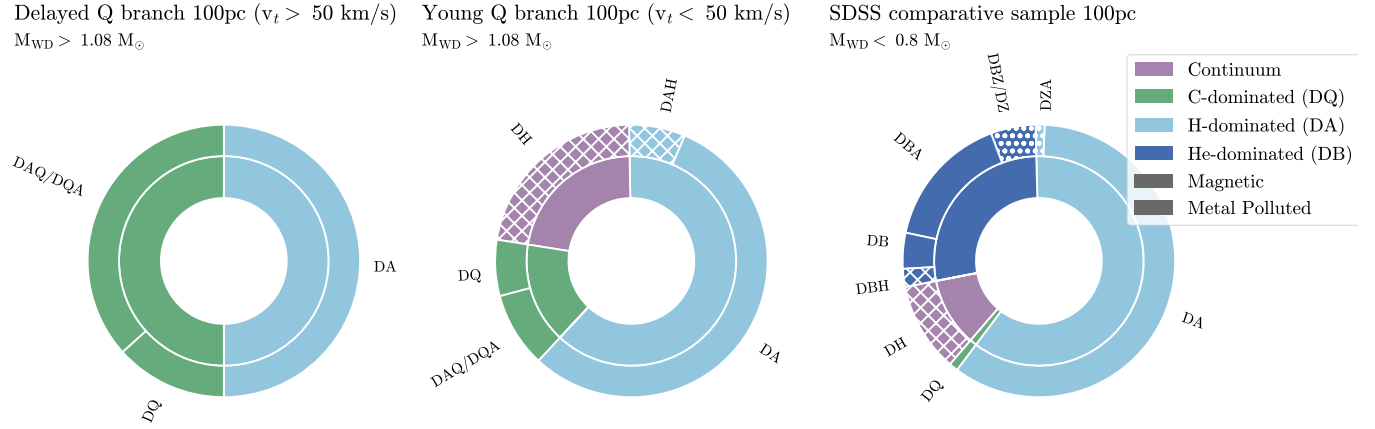


**Figure 2.** Sunburst plot of the spectral type distribution for each of the two kinematically selected subsets in the Q branch region and a comparison sample: the delayed Q branch subset ( $v_t > 50 \text{ km s}^{-1}$ ), the young Q branch subset ( $v_t < 50 \text{ km s}^{-1}$ ), and the single star evolution average mass sample from SDSS ( $M < 0.8 M_{\odot}$  and  $v_t < 50 \text{ km s}^{-1}$ ). The inner ring shows the dominant composition from spectroscopy, and the outer ring specifies the spectral type based on all elements detected in a low-resolution spectra. The physical meaning of each spectral type is described in Section 4. The delayed subset has the highest fraction of white dwarfs with carbon-dominated atmospheres. There are striking differences between the populations in the fraction of magnetism (0%, 27%, 14% respectively), helium-dominated atmospheres (0%, 0%, 28% respectively), and metal pollution (0%, 0%, 6% respectively).

“spaghetti plots”) with the Zeeman splitting tool<sup>1</sup> (Schimeczek & Wunner 2014; Inight et al. 2023). The estimated field strengths for the three DAH white dwarfs are  $B = 2.8 \text{ MG}$  for WD J050709.66+264515.13,  $B = 7.3 \text{ MG}$  for WD J133340.35+640627.35, and  $B = 4.5 \text{ MG}$  for WD J194736.29–310038.84.

Additionally, 10 white dwarfs have spectra dominated by continua, where very strong magnetism ( $\gtrsim 50 \text{ MG}$ ) has induced strong non-linear Zeeman effects on the spectrum (22% DH). We denote these as DH (which are also referred to as MWD for magnetic white dwarfs in Gentile Fusillo et al. 2021). The spectra of cooler white dwarfs ( $T_{\text{eff}} < 10,000 \text{ K}$ ) often show no absorption lines and are categorized as continuum white dwarfs (DC). But in the Q branch temperature range ( $T_{\text{eff}} \gtrsim 11,000 \text{ K}$ ), we expect hydrogen, helium, or carbon to be visible. Hence, any continuum spectrum in our sample is likely to be a strongly magnetic white dwarf (DH) (e.g., Berdyugin et al. 2023).

The overall magnetism fraction of the young Q branch subset is 27% (12/45, including DAH and DH white dwarfs). While this fraction is remarkably similar to the fraction of magnetic ultra-massive white dwarfs in Solar neighborhood (32% in Jewett et al. 2024), this is significantly higher than the field white dwarf magnetic fraction before crystallization, estimated to be  $\approx 5\%$  with

field strength  $B > 1 \text{ MG}$  (Bagnulo & Landstreet 2022; Moss et al. 2025).

#### 4.3. Comparison with canonical-mass white dwarfs

The third panel in Figure 2 reveals the spectral type distribution for field white dwarfs within 100 pc in our stellar neighborhood, the vast majority of which should result from single-star evolution (Cheng et al. 2020). Both Q branch subsets show drastic differences from the reference sample.

The first major difference is the fraction of white dwarfs with helium-dominated atmosphere. The comparison sample shows that 26 out of 94 objects have helium in their atmosphere in this temperature range (roughly  $10,000 < T_{\text{eff}} < 26,000 \text{ K}$ ), often with other elements such as hydrogen or heavy metals (28% spectral types DB, DBA, DBZ, DBAZ). But no white dwarfs in either subset of the Q branch show helium. Bédard et al. (2024) also note the lack of Q branch white dwarfs showing helium-dominated atmospheres. Beyond the Q branch, it has also been observed that massive white dwarfs rarely harbor helium-dominated atmospheres (O’Brien et al. 2024; Jewett et al. 2024; Kilic et al. 2025).

There is just one carbon-dominated atmosphere white dwarf in the low-mass sample, which is a much lower fraction of DQs than either subset of the Q branch. This is reasonable for a single star evolution subset, as there should be no carbon seen through the photosphere even assuming thin hydrogen and helium layer models (Bauer

<sup>1</sup> [https://github.com/WD-planets/Zeeman\\_splitting](https://github.com/WD-planets/Zeeman_splitting)

**Table 1.** Atmospheric Composition of Q branch white dwarfs based on low-resolution optical spectroscopy compared to an average-mass comparison sample in the same temperature range

Spectral Type	Delayed Q branch	Young Q branch	Comparative
DA	15	25	57
DAH	0	3	0
DQ	4	3	1
DQA	6	3	0
DAQ	5	1	0
DH	0	10	10
DB <sup>*</sup>	0	0	26
Magnetic	0	12	13
Metal Polluted	0	0	6
<b>Total</b>	<b>30</b>	<b>45</b>	<b>94</b>

\*Also includes DBA, DBAH, DBH, DBZ, and DBAZ spectral types.

et al. 2025), and convection does not explain the presence of DQ white dwarfs for  $T_{\text{eff}} > 10,000$  K (e.g., Blouin et al. 2023).

Magnetism is detected in 13 white dwarfs of the comparison sample, split between continuum white dwarfs (DH, 10/94), and helium-dominated atmosphere white dwarfs with Zeeman splitting (DBH, 3/94).

The last difference to note is the presence of six white dwarfs with photospheric metals in the comparative sample (6%, spectral types DZ, DBZ, DZA). Metal pollution is inferred from photospheric transitions of heavy elements (such as calcium, iron, or magnesium) and implies the presence of remnant planetary systems, which are common around average-mass white dwarfs (e.g., Koester et al. 2014). We do not detect accreted metals in either subset of the Q branch, possibly tied to the non-detection of helium-dominated white dwarfs on the Q branch since it is easier to detect metals in DB white dwarfs. The implications for planetary survival around Q branch white dwarfs are discussed in Section 6.3.

It should be noted that this is not a spectroscopically complete sample, but was selected randomly from serendipitous SDSS spectroscopy, and it should reasonably approximate the underlying population given this reasonably hot temperature range.

## 5. PHOTOMETRIC VARIABILITY ON THE Q BRANCH

Double-degenerate merger remnants are expected to rotate rapidly, having conserved angular momentum from previously being in a compact binary. Theoretical models suggest that WD+WD byproducts should ro-

tate on the order 10 – 20 minutes (Schwab 2021), much faster than white dwarfs resulting from single-star evolution, which should rotate at periods around 1 d (Hermes et al. 2017; Fuller et al. 2019). We investigate the photometric variability of the objects in our sample as seen by ground-based time-domain surveys to flag any with short-period ( $P < 2$  hr) variability that could be caused by surface spots that reveal the stellar rotation rate (e.g., Steen et al. 2024). We targeted flagged objects with follow-up time-series photometry to verify their variability and also observed objects whose survey photometry is poorly constraining.

### 5.1. Time-Series Photometry

#### 5.1.1. Survey Photometry

We query photometry from the Transiting Exoplanet Survey Satellite (TESS; Ricker et al. 2015), the Zwicky Transient Facility (ZTF; Masci et al. 2019) and the Asteroid Terrestrial-impact Last Alert System Survey (ATLAS; Tonry et al. 2018) to search their corresponding Lomb-Scargle periodograms (Lomb 1976; Scargle 1982) for periodic variability. More precisely, we utilize the PDCSAP flux from the 2-minute and 20-second TESS-SPOC photometry for our search. Our ZTF photometry is sourced from public Data Release 23, which we query on the J2016.0 Gaia DR3-measured centroids using a 3.5'' circular aperture. And we use the ATLAS difference images, queried on the same centroids propagated on the Gaia-measured proper motions.

For each light curve, we compute PSD-normalized Lomb-Scargle periodograms using `astropy` (Astropy Collaboration et al. 2013, 2018, 2022). This includes partitioning the ZTF and ATLAS photometry by color, treating the  $g$ ,  $r$ , combined  $g+r$ , and  $c$ ,  $o$ ,  $c+o$  photometry independently. We bootstrap 0.1% false-alarm probability thresholds with replacement over 10,000 iterations to vet these light curves for periodic variability (c.f., VanderPlas 2018).

We recover light curves for 74 out of the 75 objects in our full Q branch sample. The only target lacking reliable time-series photometry is WD J115618.17–675029.94; field crowding ruins the fidelity of its ATLAS images, preventing any reliable analysis. No objects show significant periodic variability in their TESS photometry at periods shorter than 2 hr. 10 unique objects show periodic significant variability in at least one of their ZTF combined  $g+r$ ,  $g$ , and  $r$  light curves. We tabulate these objects and the detected periodicities and amplitudes in Table B1. We exclude detections of peaks at the daily alias and its respective harmonics.

### 5.1.2. Follow-up High-Speed Time-Series Photometry

We conducted follow-up campaigns that observed 25 rapid-rotator candidates with ground-based, high-speed, time-series photometry. We specifically targeted those objects that showed significant or near-significant variability in their survey photometry and those with poor bootstrapped NOV limits ( $\gtrsim 1\%$ ). We observed 18 targets at the 2.1-meter Otto Struve Telescope at McDonald Observatory using the ProEM frame-transfer CCD mounted at Cassegrain focus, another five targets at the 1.8-meter Perkins Telescope Observatory (PTO) using the Perkins Re-Imaging SysteM (PRISM; [Janes et al. 2004](#)) mounted at Cassegrain focus, and three additional targets at the 4.3-m Lowell Discovery Telescope (LDT) using the Large Monolithic Imager (LMI). The respective plate scales for our observations are  $0.36''$  for ProEM,  $0.39''$  for PRISM, and  $0.36''$  with LMI at  $3\times 3$  binning. We include our observing log in Table B2. All images were reduced using standard Python-based routines with bias, dark (ProEM only), and flat-field calibration images and the Astropy-affiliated `ccdproc` ([Craig et al. 2017](#)) suite of tools. We performed PSF photometry using `hipercam` ([Dhillon et al. 2021](#)) and used `phot21c` ([Vanderbosch 2023](#)) to extract the optimal light curve. We refer readers to [Guidry et al. \(2025\)](#) for a more detailed description of this reduction and light curve extraction process, which we emulate here for each facility.

We similarly period search these follow-up photometry, again computing PSD-normalized Lomb-Scargle periodograms and bootstrapping 0.1% false-alarm probability significance thresholds with replacement over 10,000 iterations. For the seven objects where periodic variability is detected, we fit sinusoids at those significant frequencies to the time series using `pyriod` ([Bell 2022](#)). We report the best-fit frequencies and associated amplitudes in Table B2. We also report there the bootstrapped significance thresholds for all objects, including those not observed to vary (NOV). We expand on the results of this analysis in the subsequent sections.

## 5.2. Rapid Rotators

We find five rapidly rotating white dwarfs with periods under 2 hr. All five new rapid rotator candidates are part of the young Q branch subset ( $v_t < 50 \text{ km s}^{-1}$ ). Their light curves and associated Lomb-Scargle periodograms are shown in the Appendix (see Figure B.2).

- WD J002959.00+364834.86 (spectral type DA) shows photometric variability at 65.76 min (0.44% amplitude), and no strong magnetism is detected spectroscopically.

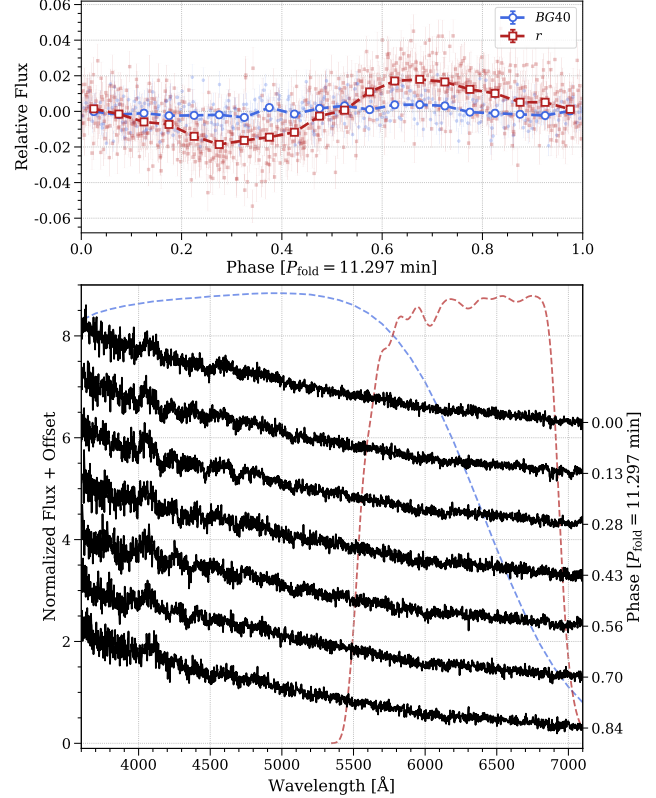


**Figure 3.** Comparative analysis of the variability detected for WD J145902.72-041157.75. Top: McDonald/ProEM light curves collected on 2025 January 30 (*BG40*, blue circles) and 2025 January 31 (*r*, red squares), all folded in phase on the rotation period of 11.297 min. We overplot binned light curves with respective integration times of 300 s and 200 s for the *BG40* and *r* photometry. Bottom: Time-resolved LDT/DeVeny spectroscopy taken on 2025 August 17. We co-add spectra within phase bins of width 0.05. The right-side y-axis ticks track the phase of the 11.297 min period relative to the start time of the 2025 January 30 light curve. The response curves of the *BG40* and *r*-band filters are plotted as dashed blue and red lines, respectively, both arbitrarily scaled. Our LDT/DeVeny spectra rule out variations at H $\alpha$  driving the 11.297 min period observed exclusively in the *r*-band, suggesting variations in the continuum flux from strong magnetism.

- WD J062535.30+190244.00 shows photometric variability at 11.05 min (0.49% amplitude) and is a strongly magnetic DH. The periodogram shows a signal at what is likely the second harmonic of the 11-min fundamental, indicating a non-sinusoidal light curve.
- WD J145902.72-041157.75 shows photometric variability at 11.297 min (1.51% amplitude) and is a strongly magnetic DH. The periodogram shows a harmonic of the 11-min signal, indicating a non-sinusoidal light curve. This target only shows sig-

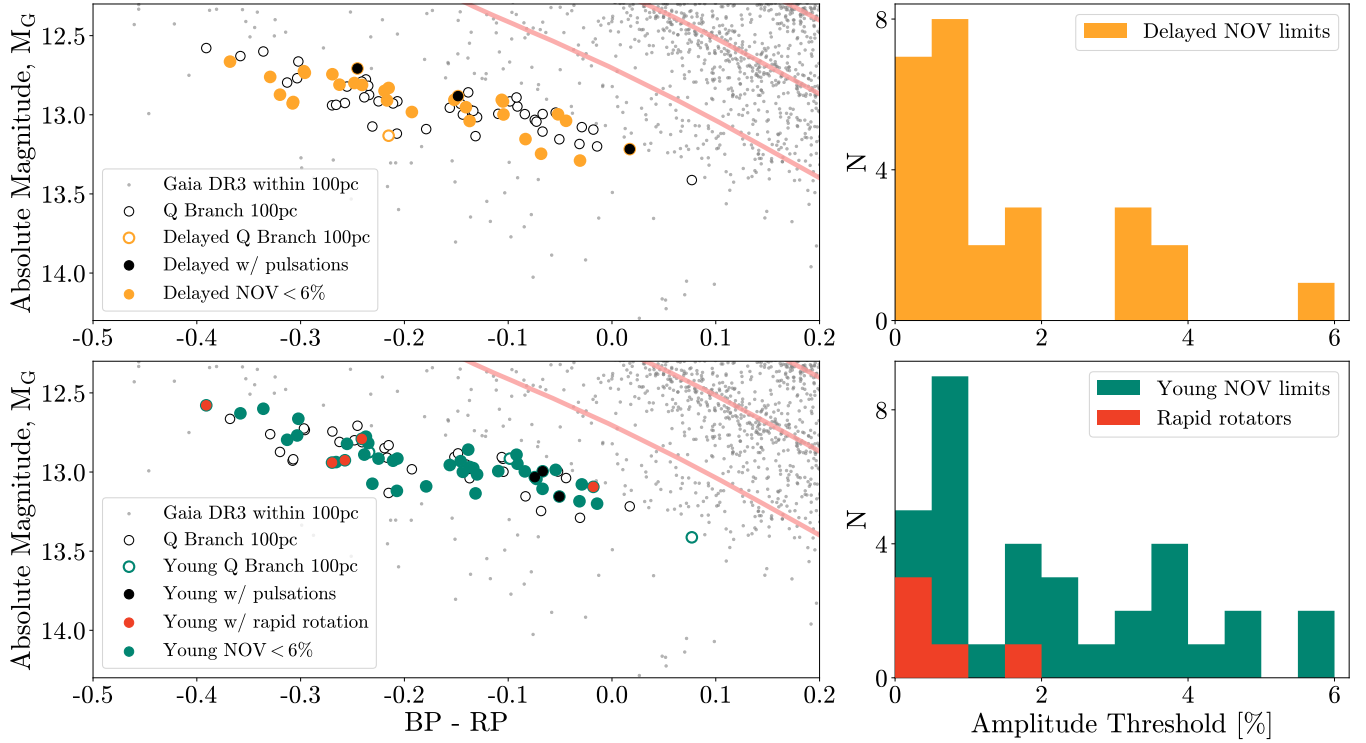


**Figure 4.** White dwarfs with rapid rotation and pulsation among the delayed and young Q branch subsets. The left panel shows color magnitude diagrams of the delayed subset (top) and the young subset (bottom) highlighting the targets for which we were able to acquire reliable time-resolved photometry based on bootstrapped NOV limits  $< 6\%$  (filled targets). The red targets show the spotted white dwarfs with detected periods under 2hr, and their observed optical amplitudes are shown in the right panel (red histogram). The black targets show the white dwarfs with pulsations, as described in Section 5.3. The right panel shows the bootstrapped NOV limits for the non-variable objects in the delayed subset (top) and the young subset (bottom). All values are reported Table C1.

nificant variability on the red (filter SDSS- $r$ ) and is further explored with time-resolved spectroscopy from LDT/DeVeny as shown in Figure 3, which suggests that the variations in the continuum flux from strong magnetism cause the variability rather than variations at H $\alpha$ .

- WD J162157.79+043218.81 shows photometric variability at 36.40 min (1.0% amplitude) and is a strongly magnetic DH. Transparency variations complicate the low-frequency region of the periodogram, where there are significant periodicities which could be more fundamental at 1/2 and 2 times this reported period. We inflate our uncertainties on the period for this object given the short dataset.
- WD J230844.31+034719.66 (spectral type DQA) has a period of 104.85 min (0.5% amplitude), and no strong magnetism is detected spectroscopically. Our 4-hr run covers less than 2.5 cycles, but the periodogram is best explained by a long-period signal and its first harmonic.

While two of the rapid rotator candidates do not show strong magnetism (WD J002959.00+364834.86 and WD J230844.31+034719.66), these white dwarfs are likely to be weakly magnetic spotted white dwarfs to explain the variability. There are poor constraints on the field strength required for spots to emerge on the surface of the white dwarfs (Maoz et al. 2015; Hallakoun et al. 2018). Figure 4 shows a color-magnitude diagram for the delayed and young subsets of the Q branch sample which spotlights our photometric variability analysis. We highlight the distribution of rapid-rotator candidates in the young subset along with the distribution of the pulsator candidates in both subsets. We also show the distribution of reliable bootstrapped NOV limits for the targets in both samples that were not observed to vary, put in the context of the amplitudes detected for rapid rotators in the young Q branch subset.

The detection of five rapidly rotating white dwarfs in the young subset of the Q branch is noteworthy (14% of the young subset). It implies that the objects of the young subset do not all result from single-star evolution. We are still limited by observational sensitivity biases,

which can be seen from the fact that the typical amplitudes of the rapid rotators in Figure 4 still falls well below many of our NOV limits. Thus, the detection of 14% rapid rotators in the young subset is a lower limit. Additionally, the relative lack of rapid rotators in the delayed population is notable considering that our NOV limits are roughly equivalent across both samples (the median limit of the delayed population is 0.91%, compared to 2.01% for the young subset).

### 5.3. Pulsating White Dwarfs

There are four previously known pulsators among the Q branch sample, which all have notable characteristics. The reported effective temperatures of the following white dwarfs rely on atmospheric modeling detailed in [Jewett et al. \(2024\)](#).

- WD J013517.57+572249.29 is a  $T_{\text{eff}} = 12,420 \pm 160$  K DA with normal kinematics that was reclassified from 7.8% NOV in [Vincent et al. \(2020\)](#) as pulsating since it shows multi-periodic oscillations by [De Gerónimo et al. \(2025\)](#). With 19 pulsation modes, it is the richest pulsating hydrogen-atmosphere ultra-massive white dwarf known to date.
- WD J055134.45+413529.95 is the first published DAQ, discovered by [Hollands et al. \(2020\)](#), and is included in our young subset, though it has extremely high space motion given its fast radial velocity; it is also likely a merger remnant.
- WD J162659.59+253326.79 is a  $T_{\text{eff}} = 13,200 \pm 190$  K DA with normal kinematics that was reclassified from 5.8% NOV in [Vincent et al. \(2020\)](#) as pulsating since it shows multi-periodic oscillations by [Jewett et al. \(2025\)](#), who also note that this object appears as an outlier compared to expected period-temperature relation for white dwarfs in the DAV instability strip. It is the hottest variable white dwarf in their sample with an exceptionally long period (1446  $\pm$  27 s period) (c.f., [Mukadam et al. 2006](#)).
- WD J165915.38+661032.66 (GD 518) is a  $T_{\text{eff}} = 11,420 \pm 110$  K DA in the delayed subset which was discovered to pulsate by [Hermes et al. \(2013\)](#) and has fast kinematics ( $v_t = 59.2 \text{ km s}^{-1}$ ), indicating it is likely a merger remnant.

At least two of the four previously known pulsators in our sample are consistent with originating from a stellar merger but do not show strong magnetism in their low-resolution spectra. Additionally, observed pulsations

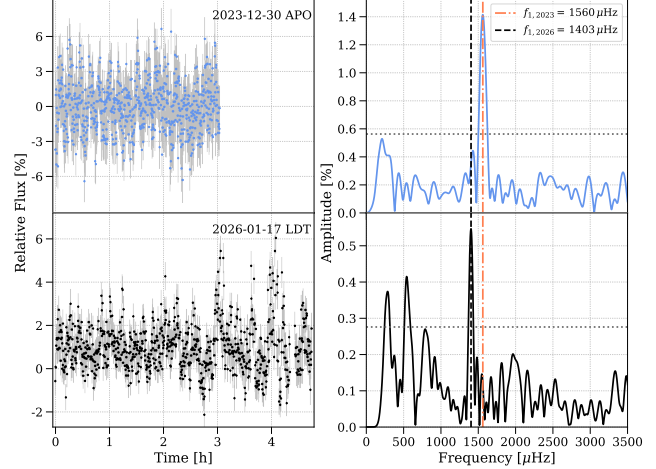


**Figure 5.** Variability of the DAQ WD J083135.57–223133.63 due to pulsations rather than rapid rotation. We show light curves from 2023 December (originally published by [Kilic et al. 2024; BG40](#), blue points) and 2026 January (*g*-band, black points) on the left panels. We show the associated Lomb-Scargle periodograms of these light curves on the right panels. The horizontal gray dotted lines delineate bootstrapped 0.1% false-alarm probability thresholds. The dashed-dotted orange vertical line maps to  $1560 \mu\text{Hz}$ , the frequency of the significant peak circa 2023 December, while the black dashed line corresponds to  $1403 \mu\text{Hz}$ , the frequency of the significant peak detected in our 2026 January LDT photometry. This period change is inconsistent with a spot and must be due to pulsations, as seen in [Hollands et al. \(2020\)](#). There are no significant frequencies beyond  $3500 \mu\text{Hz}$ .

imply a low surface magnetic field (less than 50 kG) as strong magnetism would suppress convection and prevent pulsations from being driven (e.g., [Rui et al. 2024](#)). These merger remnants must originate from an evolution pathway that does not generate strong magnetism.

There are two additional rapid-rotator candidates in the delayed Q branch subset (the DAQ WD J083135.57–223133.63 and the DAQ WD J234043.98–181945.62) identified in [Kilic et al. \(2024\)](#) as having photometric variability driven by surface spots. However, our follow-up observations of both targets show periods inconsistent with those previously reported. Observing incoherence in mode amplitudes is characteristic of non-radial pulsations (e.g., [Hermes et al. 2017](#)), so we reclassify WD J083135.57–223133.63 and WD J234043.98–181945.62 as pulsating white dwarfs. The most recent period is 712.91 s for WD J083135.57–223133.63, and 803.46 s for WD J234043.98–181945.62. Figure 5 and Figure 6 show the period change between the observations from [Kilic et al. \(2024\)](#) and our recent follow up from LDT/LMI. In the LDT/LMI follow-up of WD J234043.98–181945.62,

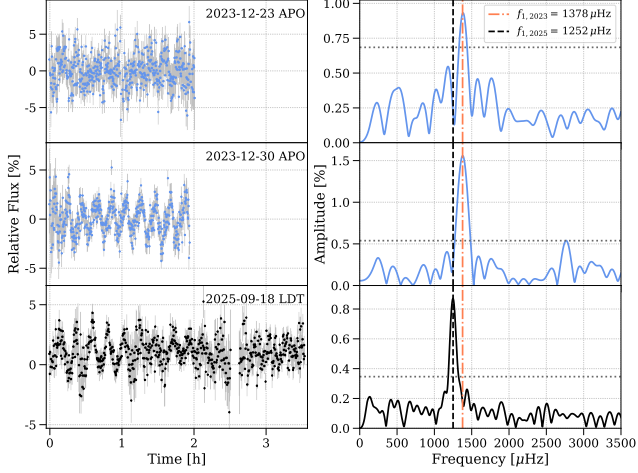


**Figure 6.** Variability of the DAQ WD J234043.98–181945.62 due to pulsations rather than rapid rotation. We plot these light curves and associated Lomb-Scargle periodograms in the same fashion as in Figure 5; the blue points are *BG40* photometry from 2023 December originally published by Kilic et al. (2024), and the black data represent novel LDT/LMI *g*-band photometry. We observe a stark change in the periodogram, where the dominant mode at  $1378\text{ }\mu\text{Hz}$  (dashed-dotted orange vertical line) disappears and one appears at  $1252\text{ }\mu\text{Hz}$  (black dashed vertical line), confirming these are pulsations and not a modulation due to a surface spot. There are no significant frequencies beyond  $3500\text{ }\mu\text{Hz}$ .

we notably detect two significant frequencies that are closely spaced:  $1252.3 \pm 2.8\text{ }\mu\text{Hz}$  and  $1275.5 \pm 4.4\text{ }\mu\text{Hz}$  (Table B2), reminiscent of the pulsation spectrum of WD J055134.45+413529.95 (Uzundag et al. 2025).

These two new pulsators are part of the delayed subset and classified as a DAQ white dwarf, which means that at least three out of the seven known DAQ within 100 pc are observed to pulsate. The remaining four DAQs within 100 pc are WD J020549.70+205707.96 (NOV 0.63%), WD J052950.25+523953.39 (NOV 0.2%), WD J065535.29+293909.66 (NOV 0.41%), and WD J170145.15–524609.22 (NOV 3.96%, from ATLAS photometry). We discuss the implications of these detections for the DAV instability strip in Section 6.4.

## 6. MERGER HISTORY OF Q BRANCH WHITE DWARFS

Our observational analysis of kinematically selected subsets of the Q branch region highlight two distinct populations of ultra-massive white dwarfs. We now connect those differences to merger history pathways.

### 6.1. Delayed *Q* branch white dwarfs are not consistent with double-degenerate merger remnants

The white dwarfs in the Q branch region with high cooling delays characterized by fast kinematics ( $v_t > 50\text{ km s}^{-1}$ ) do not follow our expectation of WD+WD merger remnants. Theoretical models of double-degenerate mergers imply rapid rotation periods and induced strong magnetism (Schwab 2021; García-Berro et al. 2012). Binary population synthesis finds the dominant binary merger type to produce massive white dwarfs ( $M_{\text{WD}} > 0.9\text{ M}_{\odot}$ ) is double white dwarf mergers (about 45%; Temmink et al. 2020). We argue that the lack of magnetism in the kinematically delayed anomalous Q branch population could be incompatible with WD+WD mergers.

#### 6.1.1. *No Strong Magnetism*

Strongly magnetic white dwarfs (field strength greater than 1 MG) are often found to have masses greater than average white dwarfs (Silvestri et al. 2007; Kawka et al. 2007). Differential rotation induced during double-degenerate mergers can produce strong, long-lived magnetic fields, of the order  $10^7\text{ G}$ , confined to the outer layers of the merger product (García-Berro et al. 2012). Population synthesis shows that the observed fraction of massive high-field magnetic white dwarfs can be explained by double degenerate stars that merge after common envelope evolution (Briggs et al. 2015).

Massive, strongly magnetic white dwarfs tend to have short rotation periods and are consistent with the double degenerate merger channel (Wickramasinghe & Ferrario 2000; Ji et al. 2013; Caiazzo et al. 2021; Hernandez et al. 2024). Strong magnetism can affect the rotation period by spinning down the star on short timescales which depend on stellar winds during the giant phase in the case of misalignment of rotation and magnetic axes (García-Berro et al. 2012; Cheng & Takata 2025). What this implies is that strongly magnetic white dwarfs without rapid rotation may still be WD+WD merger remnants.

Still, none of the 30 delayed white dwarfs on the Q branch within 100 pc show strong magnetism, to a limit of at least 1 MG, which suggests that the merger pathways leading to these white dwarfs do not drive strong dynamos.

Finding no evidence of strong magnetism for the delayed white dwarfs with carbon atmospheres (spectral types DQ, DQA, DAQ) contrasts with the large fraction of magnetic hot DQ white dwarfs (Dunlap & Clemens 2015) which reside above the Q branch (at least 70% of hot DQs are strongly magnetic; Dufour et al. 2013; Coutu et al. 2019). This could imply that hot DQs evolve into warm DQ in the young subset rather than the delayed subset. Furthermore, the fraction of mag-

netism in the young subset of the Q branch subset is consistent with a double-degenerate merger origin.

But strong magnetism in merger products can also be tied to the mass ratio of the progenitors. [Pakmor et al. \(2024\)](#) shows that unequal-mass merger remnants may produce an extra convection zone in the region that contains most of the magnetic energy, which could destroy the strong, ordered field. They test this phenomenon by simulating double-He-core white dwarfs mergers with a total mass of  $0.6 M_{\odot}$ . The white dwarfs in the delayed subset of the Q branch are ultra-massive, so the specific merger channel in that study could not produce the objects of our sample. Further simulations are required to observe the effects of unequal-mass mergers on double-C/O-core white dwarfs with total mass greater than  $1.05 M_{\odot}$  and a C/O-core white dwarf with a He-core white dwarf mergers with total masses up to  $1.2 M_{\odot}$ . Still, in the case where the mechanism of magnetic field suppression applies to other merger channels, the observed lack of strong magnetism could suggest that the Q branch white dwarfs of the delayed subset are produced from unequal-mass mergers.

#### 6.1.2. No Evidence of Rapid Rotation

We expect the product of double-degenerate mergers to be rapid rotators. The merger remnant carries the angular momentum from the point of tidal disruption where the binary is at a short orbital period (orbital separations under 1 hour, e.g., [Ferrario et al. 1997](#); [Reding et al. 2020](#)). From 1D stellar evolution models of WD+WD mergers, the prediction is for the remnant to reach a characteristic minimum angular momentum after the giant phase, which is then retained assuming conservative evolution. As such, the final products should be white dwarfs with rotation periods of order  $10 - 20$  min ([Schwab 2021](#)).

We do not detect rapid rotation via spots for any of the white dwarfs in the delayed kinematic subset of the Q branch region to a median NOV limit of 0.91%. The typical amplitudes of the modulations observed at rapidly rotating ultra-massive white dwarfs tend to be lower than this value ( $A \approx 0.7\%$  from recently discovered rotators in [Williams et al. 2025](#) with the same setup as most of our follow-up observations).

Using the same sensitivity in all of our photometric study, we were still able to detect five rapid rotators in the young subset. Given our NOV limits and the typical amplitudes of rapid rotators, we expect that the young subset harbor many more rapid rotators that we do not have the sensitivity to detect. When accounting for the median amplitude of the detected rapid rotators in our sample which is 0.5%, we can compare the rapid rotation

detections in both subsets limited to NOV limits under 0.5%. While this yields extremely small number statistics, it sets a  $1-\sigma$  upper limit of rapid rotation of 14% rapid rotation in the delayed subset (0/10), compared to a rapid rotation fraction of  $50\%^{+18}_{-15}$  (5/10). This demonstrates that the observed lack of rapid rotation within the delayed population is significant. In order to present quantifiable occurrences of the rapid rotation in either subset, better limits are necessary.

The lack of photometric variability from spots should not be treated independently from the observed lack of strong magnetism, because spots should only be detectable in the presence of weak magnetism, though the exact field strength necessary remains unconstrained ([Maoz et al. 2015](#); [Hallakoun et al. 2018](#)). Yet, our analysis provides further evidence that the white dwarfs in the delayed Q branch subset within 100 pc are not strongly magnetic, and perhaps inconsistent with WD+WD merger remnants.

#### 6.1.3. Possible Magnetic Field Decay

The kinematics of the white dwarfs in the delayed subset of the Q branch reveal older ages than predicted from theoretical cooling tracks. As white dwarfs evolve along cooling tracks, magnetism is observed to emerge, resulting in cool older white dwarfs showing a higher fraction of magnetism than young white dwarfs ([Bagnulo & Landstreet 2022](#)).

The fate of double-degenerate mergers has been modeled on relatively short timescales (e.g. [Yoon et al. 2007](#); [Shen et al. 2012](#)). Still, we have poor constraints on the evolution of the field strength as a magnetic white dwarf merger remnant cools. Isolated white dwarfs are expected to see magnetic field decay from ohmic dissipation by a factor of two in 10 Gyr ([Fontaine et al. 1973](#); [Wendell et al. 1987](#)). Depending on the initial strength of the magnetic field, dissipation can also be driven by Hall drift for fields  $10^{12} \text{ G} < B < 10^{14} \text{ G}$ , or ambipolar diffusion for fields  $B \gtrsim 10^{14} \text{ G}$  ([Heyl & Kulkarni 1998](#)). Magnetic field decay and thermal cooling effects may impact the thermal characteristics and mass-radius relationship of the remnant ([Bhattacharya et al. 2022](#)).

Our observations are also compatible with magnetic field decay in double-degenerate products over multi-Gyr timescales, assuming magnetism was induced at the time of merger. The distillation process causing the high cooling delays triggers turbulence within white dwarf cores which may last for billions of years ([Lanza et al. 2024](#)), and turbulence enhances magnetic diffusivity, which may accelerate the decay of existing magnetic fields ([Castro-Tapia et al. 2024](#)). Further modeling is necessary to constrain magnetic decay decoupled

from thermal cooling. If magnetic field decay can be shown to be insignificant, that would point to a scenario where white dwarfs with cooling delays in the Q branch arise from a merger channel with no induced magnetism, likely ruling out the double-degenerate merger scenario.

### 6.2. *Q branch white dwarfs must be merger remnants*

Even if Q branch white dwarfs with high cooling delays are inconsistent with the double-degenerate merger scenario, a stellar merger must be producing these objects, so other merger histories should be considered.

While cool white dwarfs ( $T_{\text{eff}} < 10,000$  K) with atomic or molecular carbon features can be explained by the dredge-up of carbon from deeper layers after convection kicks in, the same process does not apply to warmer white dwarfs. A different evolutionary pathway is required to produce warm and hot DQs, and growing evidence suggests a merger origin (Dunlap & Clemens 2015; Williams et al. 2016; Coutu et al. 2019; Kawka et al. 2023).

Our photometric analysis of the delayed Q branch subset is compatible with the prediction of Shen et al. (2023) for the cooling anomaly white dwarfs to be the product of a C/O-core white dwarf and the He-rich core of a subgiant, though the expected product of such a merger is relatively unconstrained. Because the orbital distance is wider for a white dwarf and subgiant at the time of merger than for WD+WD binaries, it is reasonable to assume that the angular momentum carried through will not be as high, resulting in longer rotation rates for the merger remnant. This could explain why we do not detect rapid rotation within our sensitivity limits. The mass ratio of the simulated merger in Shen et al. (2023) calls for a  $1.0 M_{\odot}$  C/O-core white dwarf with a  $0.2 M_{\odot}$  He-rich core of a subgiant. The extreme unequal-mass of this merger channel could also help explain the lack of strong magnetism (Pakmor et al. 2024).

The high cooling delays observed on the Q branch require super-solar abundances to lead to the distillation process. So far, the only non-isolated-white-dwarf scenario which reproduces the requisite metallicities able to drive long cooling delays is the merger of a massive C/O-core white dwarf with a subgiant. Other merger channels, such as a C/O-core white dwarf and a He-core white dwarf, may create ultra-massive C/O-core remnants in the Q branch region but these do not produce the additional  $^{22}\text{Ne}$  necessary to explain the observed Q branch overdensity (Shen et al. 2023).

Our observations alone do not allow us to completely rule out different types of stellar mergers. It is also possible to produce anomalous ultra-massive C/O-core white dwarfs without the need of a merger (Althaus et al.

2021). Even though such white dwarfs evolve slower than the predicted O/Ne-core white dwarfs, and therefore appear older on the predicted cooling tracks, they do not recreate the high cooling delays observed in the subset of our study with fast kinematics.

### 6.3. *No Evidence of Metal Pollution*

There are no detections of photospheric metal pollution from elements like calcium or iron in optical observations around any objects on the Q branch which could imply a lack of remnant planetary systems. Although remnant planetary systems around white dwarfs are common (Koester et al. 2014), there is a  $4\sigma$  decrease in observed metal pollution for massive ( $M_{\text{WD}} > 0.8 M_{\odot}$ ) white dwarfs (Ould Rouis et al. 2024; Cunningham et al. 2025). The observed lack of remnant planetary systems on the Q branch is consistent with the previously observed discrepancy in metal pollution as a function of mass, but can also be accounted for only with observational biases. Detecting metals in the atmospheres of DA white dwarfs from lower resolution spectroscopy offers challenges and require higher resolution spectroscopy or UV spectroscopy (e.g., Gänsicke et al. 2012).

We note that one DA white dwarf in the delayed Q branch subset, WD J034703.18–180253.49, is believed to be transited by planetary debris on a highly eccentric orbit with a period of  $> 100$  d (Guidry et al. 2021). Higher-resolution spectroscopy in the ultraviolet may reveal photospheric metals on this object, so further investigation is required to fully measure the planetary occurrence on the Q branch.

The Q branch population may also help constrain if the nature of stellar merger events prevents planets from surviving as efficiently as around the isolated progenitors of canonical-mass white dwarfs. Planetary systems can form around binary systems and possibly survive the binary orbital decay within specific configurations (Muñoz & Lai 2015; Veras et al. 2018), though the stability of circumbinary orbits varies across binary mass fraction and binary eccentricity (e.g., Ballantyne et al. 2021). The dynamical evolution of planetary architecture and the conditions of instability, disruption, and engulfment for planets in interacting binaries is still a topic of active research (Xing et al. 2025), but the overall conclusion is that tidal forces at play in a merger event create instability for circumbinary planets and increase the chance of escape (Veras & Tout 2012).

Higher-resolution spectroscopy is necessary to rule out the presence of heavy elements in the DA white dwarfs of the Q branch region and comment on the remnant

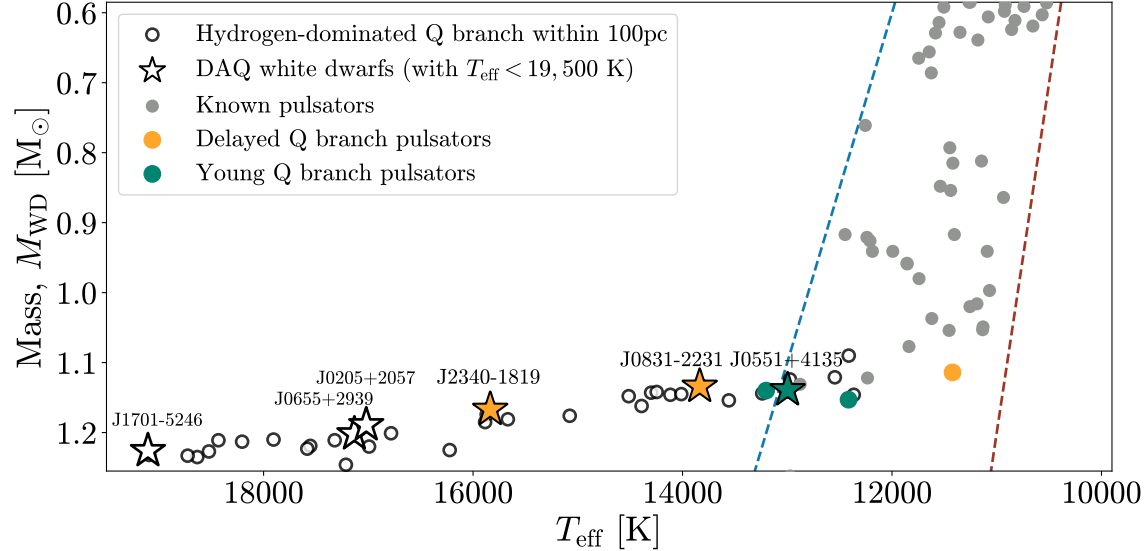


**Figure 7.** Known pulsating white dwarfs across the DAV instability strip (gray points) from Vincent et al. (2020) and Jewett et al. (2025). The pulsators of the Q branch are highlighted based on the kinematic subset they belong to (orange for delayed subset, green for young subset). The black circles show the Q branch white dwarfs with hydrogen-dominated atmospheres (spectral types DA, DAQ, DAH). The blue and red dashed lines are the empirical boundaries of the photometric DAV (or ZZ Ceti) instability strip (Vincent et al. 2020). The stars correspond to the six DAQ white dwarfs with  $T_{\text{eff}} < 19,500$  K within 100 pc, including our newly discovered target WD J170145.15–524609.22. Three DAQs within 100 pc are pulsating.

planetary system occurrence for ultra-massive merger remnants.

#### 6.4. Extended Instability Strip

Our study of pulsating white dwarfs in the Q branch region has revealed a possible extension of the DAV (a.k.a. ZZ Ceti) instability strip. The DAV instability strip refers to a parameter space ( $10,400 \text{ K} < T_{\text{eff}} < 12,400 \text{ K}$  for canonical-mass DAs) where H-dominated white dwarfs pulsate with periods ranging from 100 s to 1400 s (Córsico et al. 2019). Studies of the massive end of the strip have revealed over 20 pulsators with masses greater than  $0.9 M_{\odot}$  (Jewett et al. 2025).

Many of the pulsating white dwarfs we describe in Section 5.3 fall outside of the empirical DAV instability strip boundaries, which are drawn from Vincent et al. (2020) in Figure 7. In particular, we discover pulsations in DAQs that are substantially hotter than the hottest known DAVs, even those of high mass.

Although DAQ white dwarfs have hydrogen-dominated atmospheres, their hydrogen layers are likely substantially thinner than most DA white dwarfs (Sahu et al. 2025). Thus, it is not necessarily the case that the convective driving of hydrogen (e.g., Wu & Goldreich 1999) is responsible for exciting the observed pulsations in DAQ white dwarfs.

For example, some white dwarfs that are accreting solar abundance material in cataclysmic variables may be able to pulsate at higher temperatures, with the driving

arising from a mix of hydrogen and helium convection zones (Van Grootel et al. 2015). A stability analysis of models of carbon-atmosphere white dwarfs using a nonadiabatic approach found excited  $g$ -mode pulsations up to periods of 700 s (Fontaine et al. 2008). The first DAQ, WD J055134.45+413529.95, located within the canonical DAV instability strip, is expected to have two convection zones, one superficial zone very near the surface and another much deeper near the region where carbon transitions to hydrogen (Hollands et al. 2020).

Driving is unlikely to be very deep: pulsation periods are driven most strongly at periods close to the thermal timescale at the base of the convection zone (Brickhill 1991). Since the pulsations observed in DAQs are generally  $P < 2000$  s, as in canonical DAVs, it is likely the driving is also happening by the surface convection zone for DAQs. That pulsations are driven in the  $T_{\text{eff}} > 15,500$  K DAQ WD J234043.98–181945.62 suggests that DAQs have superficial convection at fairly high temperatures. Certainly more theoretical work is needed to understand the DAQ instability strip.

It is worth noting that the DAQs are not the hottest hydrogen-dominated white dwarfs observed to pulsate. That record is held by the so-called hot DAVs near 30,000 K (Kurtz et al. 2013; Romero et al. 2020), which are possibly driven by a superadiabatic layer in DAs with thin hydrogen layers that are at the cool end of the DB gap (Shibahashi 2007).

## 7. CONCLUSION

We conduct a volume-limited spectroscopic and photometric study of white dwarfs in the Q branch region within 100 pc to investigate an anomalous population of ultra-massive white dwarfs with high (at least 6 Gyr) cooling delays, first discovered by Cheng et al. (2019). We find significant differences in atmospheric composition and rotation rates as a function of kinematics.

White dwarfs in our delayed subset in the Q branch have fast kinematics ( $v_t > 50 \text{ km s}^{-1}$ ) indicative of high cooling delays, and show carbon-dominated atmospheres more frequently than other populations of white dwarfs, indicating the population typically has very thin hydrogen layers. We expect the ultra-massive ( $M_{\text{WD}} > 1.08 M_{\odot}$ ) delayed white dwarfs on the Q branch to have originated in a merger. However, we do not detect strong magnetism (to a limit  $>1 \text{ MG}$ ) nor rapid rotations (to amplitude limits greater than roughly 0.9%) within the delayed sample. The lack of strong magnetism for the Q branch white dwarfs with the longest cooling delays offers a puzzle regarding the merger progenitor scenario. We hypothesize that these objects may not typically arise from double-degenerate (WD+WD) mergers and instead require a merger channel which does not induce strong magnetism, though we cannot yet rule out that induced strong fields decay over the long cooling delays. Mergers of two white dwarfs with an unequal mass ratio may offer a way (Pakmor et al. 2024) to explain the lack of magnetism in these merger remnants. Our observations remain consistent with delayed Q branch white dwarfs arising from the merger channel of a C/O-core white dwarf and the He-rich core of a subgiant (Shen et al. 2023).

The Q branch white dwarfs in our young subset (with slow kinematics,  $v_t < 50 \text{ km s}^{-1}$ ) show a significantly higher fraction of strongly magnetic white dwarfs and white dwarfs detected to have rapid rotation periods, revealing that we can detect such objects in the delayed subset but that such objects are generally rare among white dwarfs with high cooling delays. The young Q branch subset reveals that there are likely WD+WD merger remnants in the Q branch region that may not exhibit extra cooling delays.

We do not detect any metal pollution within the Q branch region, which is consistent with the lack of massive white dwarfs with photospheric metals indicative of remnant planetary systems (e.g., Ould Rouis et al. 2024) though further follow up is required as low resolution spectroscopy is insensitive to the detection of heavy metals in DA white dwarfs.

While the Q branch region falls outside of the DAV instability strip boundaries at much

hotter temperatures, we report on six pulsating white dwarfs within our sample, including two DAQ white dwarf (WD J083135.57–223133.63 and WD J234043.98–181945.62) whose variability we reclassify from a spot to pulsations in this paper. While the former falls just outside of the DAV instability strip boundaries, the latter is a  $T_{\text{eff}} > 15,500 \text{ K}$  pulsating white dwarf with a hydrogen-dominated atmosphere, thousands of degrees hotter than where we expect convection to be significant enough to drive pulsations for a typical DAV, even at such a high mass (Jewett et al. 2025). That makes at least three pulsators out of the six published white dwarfs in the DAQ class within 100 pc, for which we add a seventh in this paper. More work is required to determine the driving mechanism for pulsations in DAQs, which likely harbor very thin hydrogen and helium layers.

In this work, we have constrained the observational makeup of white dwarf stars in the Q branch of the Gaia color-magnitude diagram within a large enough volume-limited sample in order to better inform the physical origin of the high cooling delays observed in a small subset (6%) of objects passing through the Q branch. Our observations remain consistent with the physical picture that the high cooling delays (at least 6 Gyr) arise from the distillation of neutron-rich species like  $^{22}\text{Ne}$ , as well as a phase separation process that creates buoyant crystals (Blouin et al. 2020a, 2021; Bédard et al. 2024). Our results prefer non-double-degenerate merger histories, so we urge future modeling to include other neutron-rich species such as  $^{26}\text{Mg}$  (Shen et al. 2023) to avoid the need for extreme and perhaps unphysical  $^{22}\text{Ne}$  abundances to explain the cooling delays with only neon. Alternative channels for the creation of delayed ultra-massive white dwarfs in the Q branch region remain possible (e.g., Fleury et al. 2023; Barrientos et al. 2025).

## 8. ACKNOWLEDGMENTS

The authors thank Jim Fuller, Evan Bauer, Boris Gänsicke, Ilaria Caiazzo, and Nicolas Rui for helpful discussions in the preparation of this manuscript. L.B.O.R. is supported by the Future Investigators in NASA Earth and Space Science and Technology (FINESST F.5) program under Award No. 80NSSC24K1549. J.A.G. is supported by the National Science Foundation Graduate Research Fellowship Program under Grant No. 2234657. This material is based upon work supported by the National Aeronautics and Space Administration under Grant No. 80NSSC23K1068 issued through the Science Mission Directorate. Support for this work was in part provided by NASA TESS Cycle 7 grant 80NSSC25K7902. This

work is supported in part by the NSF under grant AST-2508429, and the NASA under grants 80NSSC22K0479, 80NSSC24K0380, and 80NSSC24K0436.

This research is based on observations made with the SOAR telescope associated with AEON program 2025A-866543 proposed through NSF's NOIRLab, as well as observations made on the Lowell Discovery Telescope, Gemini South Telescope, and McDonald 2.1-meter Otto Struve Telescope. The authors thank the telescope operators and observatory staff for their invaluable help and assistance.

The ZTF forced-photometry service was funded under the Heising-Simons Foundation grant #12540303 (PI: Graham). This work has made use of data from the European Space Agency (ESA) mission Gaia (<https://www.cosmos.esa.int/gaia>), processed by the Gaia Data Processing and Analysis Consortium (DPAC, <https://www.cosmos.esa.int/web/gaia/dpac/consortium>). Funding for the DPAC has been provided by national institutions, in particular the institutions participating in the Gaia Multilateral Agreement. This paper includes data collected by the TESS mission. Funding for the TESS mission is provided by the NASA's Science Mission Directorate.

This research was improved by discussions at the KITP Program “White Dwarfs as Probes of the Evolution of Planets, Stars, the Milky Way and the Expanding Universe” supported by National Science Foundation under grant No. NSF PHY-1748958.

*Facilities:* ATLAS, Gaia, Gemini:South (GMOS), LDT (DeVeny, LMI), Struve (ProEM), Perkins (PRISM), PO:1.2m (Zwicky Transient Facility), SOAR (Goodman), TESS

*Software:* Astropy (Astropy Collaboration et al. 2013, 2018, 2022), astroquery (Ginsburg et al. 2019), ccdproc (Craig et al. 2017), hipercam (Dhillon et al. 2021), lmfit (Newville et al. 2025), matplotlib (Hunter 2007), numpy (Harris et al. 2020), pandas (Wes McKinney 2010; pandas development team 2024), phot2lc (Vanderbosch 2023), PypeIt (Prochaska et al. 2020a), Pyriod (Bell 2022), scipy (Virtanen et al. 2020), TOPCAT (Taylor 2011)

## APPENDIX

## A. SPECTROSCOPY

We present all 26 new spectra acquired with SOAR/Goodman, Gemini/GMOS, and LDT/DeVeny. Figure A.1 includes all 14 new DA white dwarfs, Figure A.2 includes three new DQ white dwarfs, Figure A.3 includes two new DQA white dwarfs, as well as one new DAQ white dwarf for which we include a model fit in Figure A.5, and Figure A.4 includes five new strongly magnetic DH white dwarfs, as well as one new DAH white dwarf. The observational details are described in Table A1.

**Table A1.** Observational details of the 26 new spectra we present in this work

Target	UT Date	Grating	Slit	Coverage	Exposures (N x $t_{\text{exp}}$ )	S/N	Spec. Type
<b>SOAR/Goodman 930-M2, R <math>\approx</math> 4500</b>							
WD J012709.06–575914.45	2018-10-27	930-M2	3"	3850-5550 Å	7 x 300 s	8.7	DA
WD J045533.97–005815.35	2019-12-06	930-M2	3"	3850-5550 Å	7 x 300 s	8.9	DA
<b>LDT/DeVeny DV2, R <math>\approx</math> 1500</b>							
WD J080122.81+774957.21	2020-01-19	DV2 300g/mm	1"	3000-7400 Å	5 x 300 s	10.5	DA
<b>Gemini/GMOS-S B480, R <math>\approx</math> 1500</b>							
WD J094500.96–685304.67	2024-01-23	B480	1"	3600-7000 Å	2 x 525 s	21.1	DQ
WD J095328.98–671447.92	2024-01-23	B480	1"	3600-7000 Å	4 x 300 s	22.3	DH
WD J175253.90–663452.57	2024-01-28	B480	1"	3600-7000 Å	4 x 110 s	15.8	DQ
<b>SOAR/Goodman 400-M1, R <math>\approx</math> 2000</b>							
WD J001534.13–604927.14	2025-06-05	400-M1	1"	3800-7000 Å	4 x 300 s	8.9	DH
WD J004527.50–233629.29	2025-06-08	400-M1	1"	3800-7000 Å	4 x 300 s	8.5	DQ
WD J045919.46–540320.77	2025-02-23	400-M1	1"	3800-7000 Å	4 x 480 s	9.9	DA
WD J072026.97–413924.27	2025-02-18	400-M1	1"	3800-7000 Å	4 x 480 s	14.0	DH
WD J094928.05–514958.10	2025-02-05	400-M1	1"	3800-7000 Å	4 x 480 s	10.4	DA
WD J100219.81–371352.08	2025-02-05	400-M1	1"	3800-7000 Å	3 x 300 s	16.8	DH
WD J115618.17–675029.94	2025-02-09	400-M1	1"	3800-7000 Å	4 x 480 s	11.8	DA
WD J134347.63–442902.53	2025-02-18	400-M1	1"	3800-7000 Å	4 x 480 s	9.0	DQA
WD J161556.15–395346.09	2025-02-24	400-M1	1"	3800-7000 Å	4 x 300 s	10.2	DA
WD J170145.15–524609.22	2025-02-24	400-M1	1"	3800-7000 Å	3 x 300 s	9.7	DAQ
WD J183302.73–412058.38	2025-04-01	400-M1	1"	3800-7000 Å	4 x 300 s	11.4	DA
WD J183449.52–450730.01	2025-04-14	400-M1	1"	3800-7000 Å	4 x 480 s	10.4	DA
WD J184809.11–461958.62	2025-03-27	400-M1*	1"	3800-7000 Å	4 x 480 s	9.9	DA
WD J193431.84–653025.80	2025-04-12	400-M1	1"	3800-7000 Å	4 x 480 s	8.7	DQA
WD J194736.29–310038.84	2025-03-21	400-M1	1"	3800-7000 Å	4 x 300 s	7.2	DAH
WD J204453.39–432919.16	2025-04-12	400-M1	1"	3800-7000 Å	3 x 300 s	10.6	DA
WD J205208.50–501335.57	2025-04-12	400-M1	1"	3800-7000 Å	4 x 480 s	7.6	DH
WD J212401.83–600059.54	2025-04-23	400-M1	1"	3800-7000 Å	4 x 480 s	11.7	DA
WD J215201.03–724022.50	2025-03-22	400-M1	1"	3800-7000 Å	4 x 300 s	9.5	DA
WD J230658.73–290514.86	2025-06-05	400-M1	1"	3800-7000 Å	4 x 300 s	9.7	DA

NOTE—All SOAR/Goodman 400-M1 use the Red camera unless noted \* if using the Blue camera. We derive S/N ratios by dividing the mean spectrum flux by the spectrum standard deviation in a 200 Å window around 4600 Å.

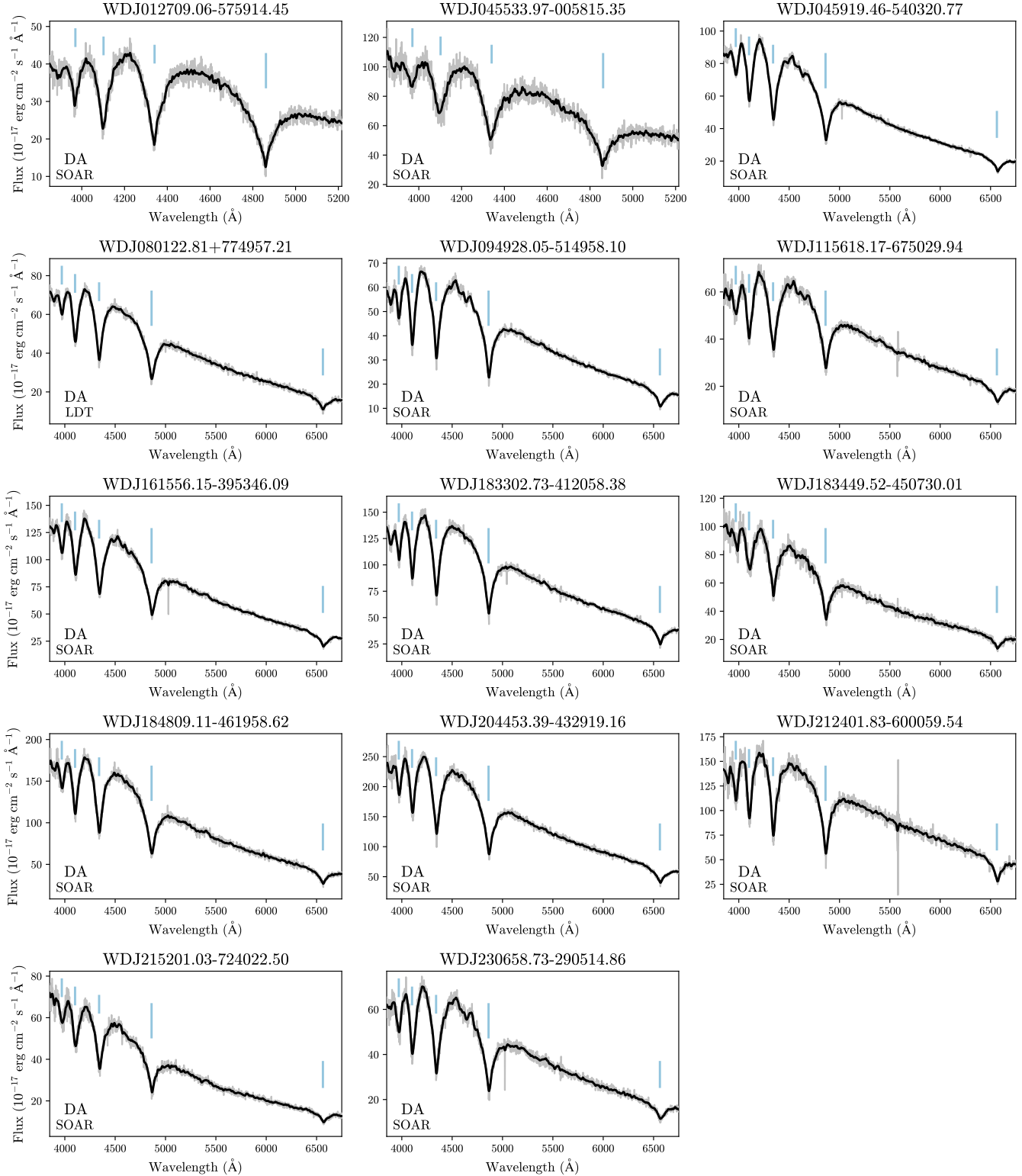


**Figure A.1.** Spectra from SOAR/Goodman and LDT/DeVeny of 14 new DA white dwarfs, with the Balmer lines indicated by the blue ticks above each spectrum.

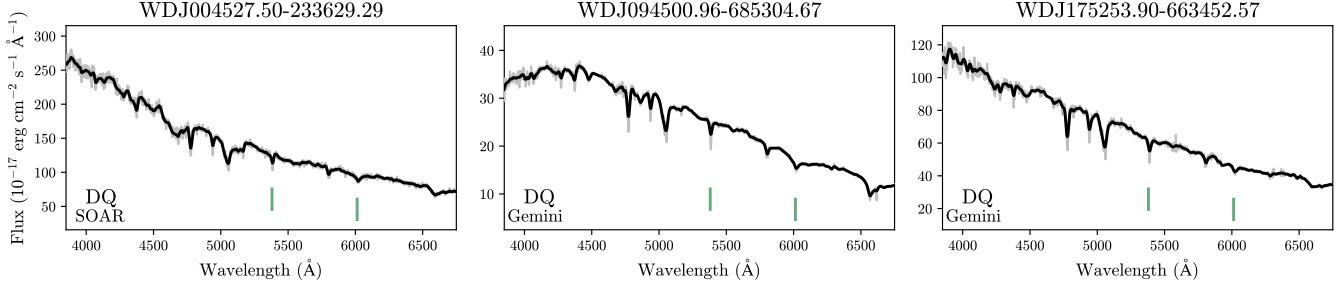


**Figure A.2.** Spectra from SOAR/Goodman and Gemini/GMOS of three new DQ white dwarfs, with strong C lines indicated by the green ticks below each spectrum.

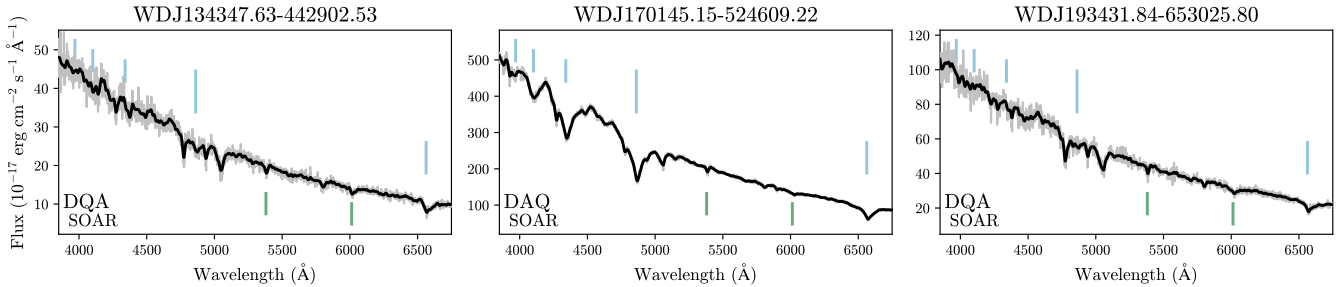


**Figure A.3.** Spectra from SOAR/Goodman of two new DQA white dwarfs as well as one new DAQ white dwarf, with Balmer lines indicated by the blue ticks above each spectrum and strong C lines indicated by the green ticks below each spectrum.

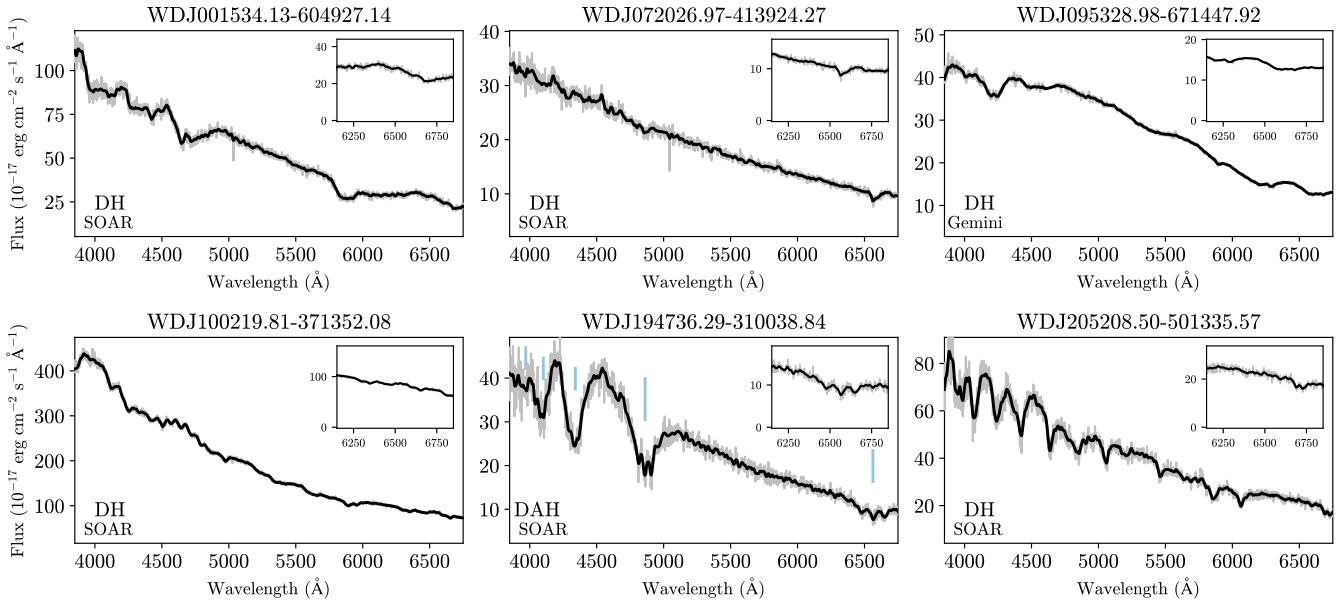


**Figure A.4.** Spectra from SOAR/Goodman of five new DH white dwarfs as well as one new DAH white dwarf, with Balmer lines indicated by the blue ticks above each spectrum and insets on the H- $\alpha$  region to highlight the Zeeman splitting or the absence of absorption line.

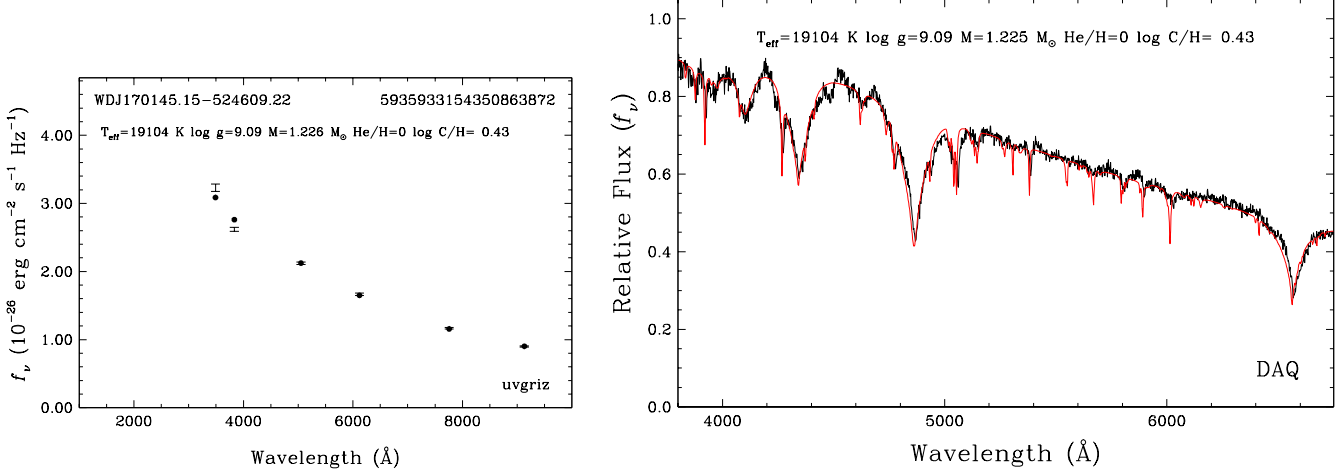


**Figure A.5.** Model fit of new DAQ WD J170145.15-524609.22 with spectral energy distribution from Skymapper photometry (left; Keller et al. 2007) and SOAR/Goodman spectrum fit (right). The best-fit parameters return  $\log C/H = 0.43$ ,  $T_{\text{eff}} = 19,104 \pm 330$  K and  $M_{\text{WD}} = 1.23 \pm 0.01$   $M_{\odot}$ . The DAQ model grids photometric fitting method is detailed in Kilic et al. (2024).

## B. PHOTOMETRY

Here we summarize all our follow-up time series photometry observations and take account of the objects that show significant periodic variability in their ZTF light curves. Table B1 includes the detected periods for 10 objects showing significant variability in at least one of the ZTF combined  $g$ ,  $r$ , or  $g+r$ , excluding objects with significant variability at the harmonics of 1 d due to aliasing. We plot the corresponding Lomb-Scargle periodograms of these systems in Figure B.1.

Figure B.2 shows the light curves and associated Lomb-Scargle periodograms for all five rapid rotator in the young Q branch sample, with Figure B.3 as its analog for the two pulsating objects in our sample. The observational details of each object is described in Table B2, where we also share a record of the entirety of our follow-up campaign.

**Table B1.** ZTF period search

Target	$N_{\text{obs}}$	$P$ s	$A$ %	Significance Threshold %
<i>g</i> -band Significant Periods				
WD J002959.00+364834.86	2060	3983.9	0.42	0.27
WD J172856.22+555822.63	1739	1838.4	0.26	0.25
WD J201115.28+491037.78	665	337.8	0.60	0.54
<i>r</i> -band Significant Periods				
WD J010413.65+465043.18	1101	4113.6	0.60	0.60
WD J013517.57+572249.29	1852	300.5	0.33	0.33
WD J145902.72-041157.75	383	680.1	1.39	0.88
WD J210547.70+590311.34	1177	6230.7	0.65	0.64
<i>g+r</i> Significant Periods				
WD J040104.29+214025.06	1130	6650.0	0.50	0.50
WD J145902.72-041157.75	653	680.1	0.73	0.60
WD J171034.72-200541.95	895	12758.2	1.06	0.91

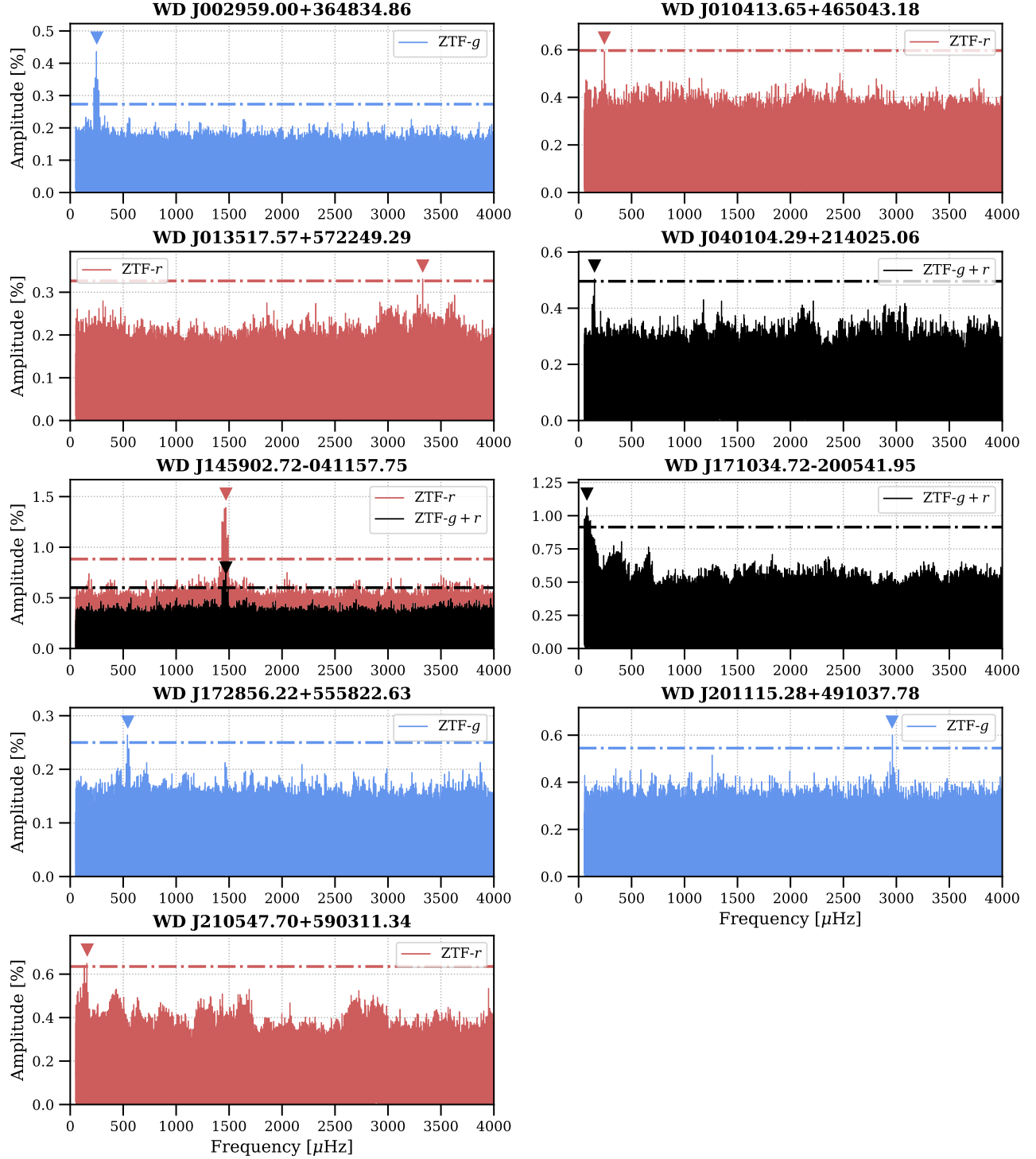


**Figure B.1.** Lomb-Scargle periodograms of all the objects that show significant periodic variability in their ZTF light curves, as detailed in Table B1. The dashed-dotted lines are the 0.1% false-alarm probability significance thresholds we bootstrapped.

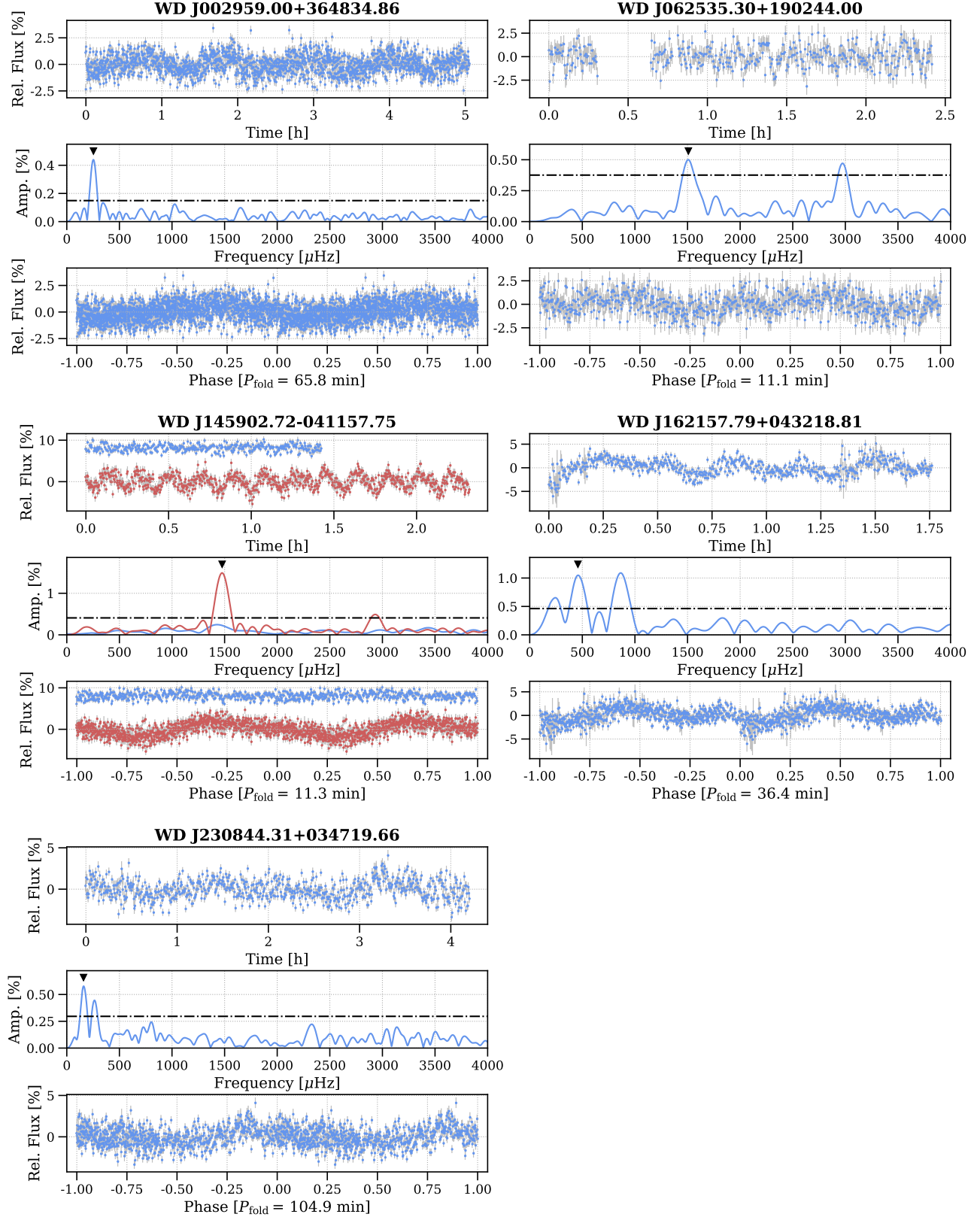


**Figure B.2.** Light curves and periodograms of all five rapid rotator candidates from the young subset of the Q branch region as described in Section 5.2. We also fold the light curves on the most dominant signal returned, marked by black triangles on the periodograms. All photometry plotted in blue were collected using a *BG40* filter, while the red were taken with the *SDSS-r* filter. The black dashed-dotted lines are the 0.1% false-alarm probability significance thresholds we bootstrapped.

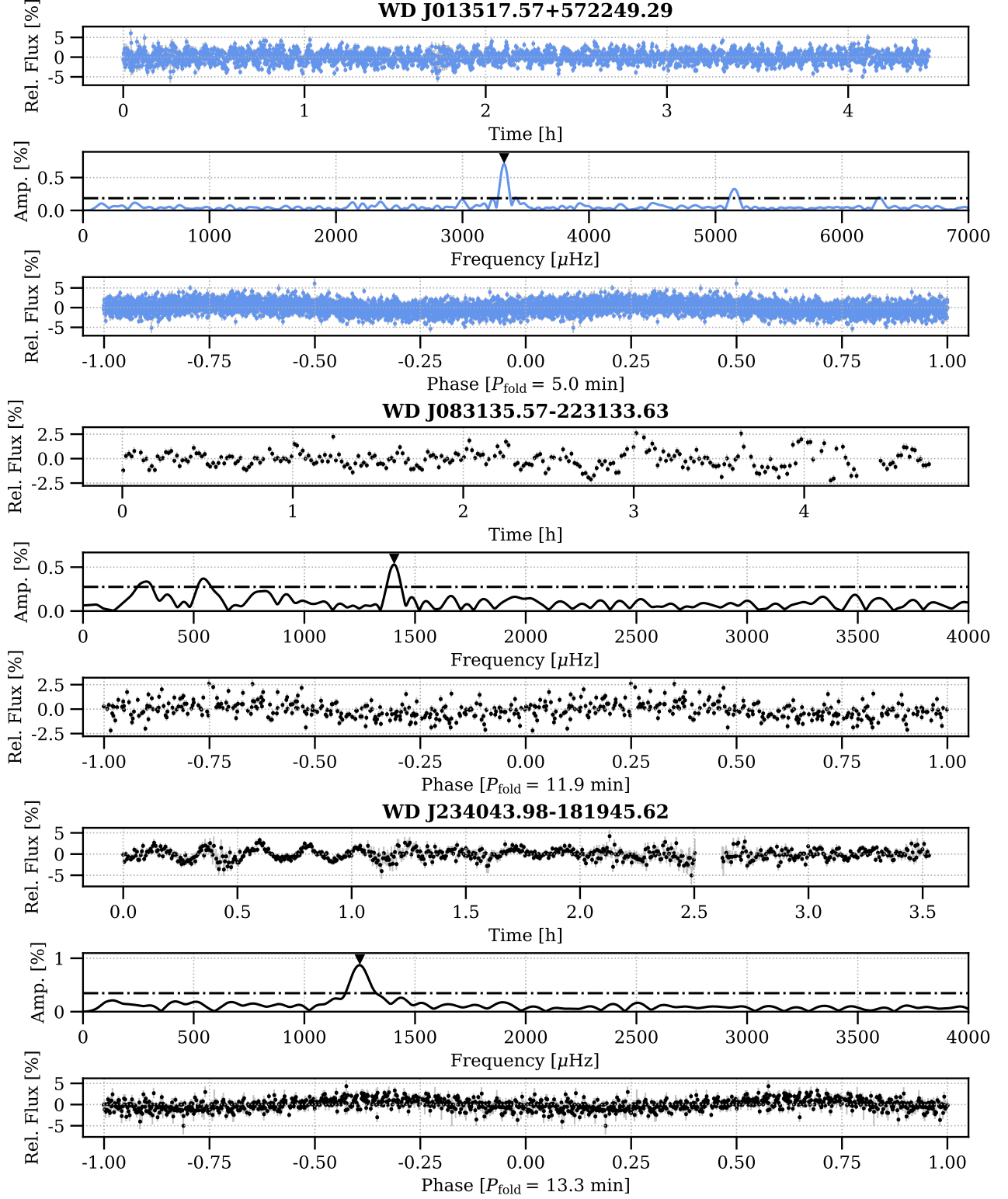


**Figure B.3.** Light curves and Lomb-Scargle periodograms of the three pulsating Q branch objects in our sample that we observed, including the newly discovered pulsating DAQs WD J234043.98–181945.62 and WD J083135.57–223133.63, all as detailed in Section 5.3. In the same fashion as Figure B.2, we also fold the light curves on the most dominant signal returned, marked by black triangles on the periodograms. All photometry plotted in blue were collected using a *BG40* filter, while the black were taken with the *SDSS-g* filter. The black dashed-dotted lines are the 0.1% false-alarm probability significance thresholds we bootstrapped. The photometry for WD J083135.57–223133.63 is binned by a factor of three to break the 1:36.5 resonance between the effective exposure time (19.53 s) and the period, which only allowed us to sample the same 73 discrete phase bins.

**Table B2.** Observing Log of Follow-up Time-Series Photometry Observations

Target	UT Date	Facility	Duration	$t_{\text{exp}}$	Filter	Seeing	$f$	$A$	S.T.	Variability
			hr	s		arcsec	$\mu\text{Hz}$	%	%	
Delayed Subset										
WD J004527.50–233629.29	2024-12-21	PTO/PRISM	2.30	25	<i>BG40</i>	3.5	–	–	0.93	
WD J010413.65+465043.18	2024-11-24	McD/ProEM	4.78	15	<i>BG40</i>	1.1	–	–	0.20	
WD J020549.70+205707.96	2024-11-26	McD/ProEM	1.75	20	<i>BG40</i>	1.9	–	–	0.63	
WD J052950.25+523953.39	2024-11-26	McD/ProEM	3.40	10	<i>BG40</i>	1.6	–	–	0.22	
WD J065335.29+293909.66	2025-01-29	McD/ProEM	1.28	10	<i>BG40</i>	2.1	–	–	0.48	
WD J080122.81+774937.21	2024-11-25	McD/ProEM	1.40	5	<i>BG40</i>	1.7	–	–	0.72	
WD J083135.57–223133.63	2026-01-17	LDT/LMI	4.74	15	<i>g</i>	3.17	$1402.7 \pm 3.5$	$0.54 \pm 0.06$	0.28	Pulsations
WD J170618.72–083747.26	2025-09-18	LDT/LMI	1.43	15	<i>g</i>	1.7	–	–	0.62	
WD J172856.22+555822.63	2025-06-28	McD/ProEM	2.56	20	<i>BG40</i>	1.0	–	–	0.70	
WD J234043.98–181945.62	2025-09-18	LDT/LMI	3.52	15	<i>g</i>	1.3	$1252.3 \pm 2.8$	$1.16 \pm 0.07$	0.35	Pulsations
							$1275.5 \pm 4.4$	$0.73 \pm 0.07$		
Young Subset										
WD J002959.00+364834.86	2024-11-23	McD/ProEM	5.04	10	<i>BG40</i>	1.0	$252.4 \pm 2.1$	$0.44 \pm 0.03$	0.15	Rapid Rotation
WD J010745.24+290420.82	2025-01-02	McD/ProEM	2.18	10	<i>BG40</i>	1.2	–	–	0.20	
WD J013517.57+572249.29	2024-11-25	McD/ProEM	4.44	5	<i>BG40</i>	1.1	$3329.1 \pm 1.8$	$0.71 \pm 0.04$	0.19	Pulsations
							$7257.2 \pm 3.4$	$0.38 \pm 0.04$		
							$5147.0 \pm 3.8$	$0.34 \pm 0.04$		
							$6297.7 \pm 6.5$	$0.20 \pm 0.04$		
WD J025001.75–043703.17	2025-01-03	McD/ProEM	1.69	15	<i>BG40</i>	1.4	–	–	0.48	
WD J062335.30+190244.00	2024-11-23	McD/ProEM	2.41	20	<i>BG40</i>	1.7	$1506.0 \pm 10.8$	$0.49 \pm 0.08$	0.86	Rapid Rotation
WD J095057.58–284115.39	2025-05-29	McD/ProEM	0.79	15	<i>BG40</i>	2.7	–	–	1.21	
WD J113502.24–243020.09	2025-03-26	McD/ProEM	1.15	30	<i>BG40</i>	1.5	–	–	7.79	
WD J133340.35+640627.35	2025-07-25	McD/ProEM	2.62	20	<i>BG40</i>	1.8	–	–	0.88	
WD J145902.72–041157.75	2025-01-30	McD/ProEM	1.42	15	<i>BG40</i>	3.4	–	–	0.29	
	2025-01-31	McD/ProEM	2.31	10	<i>r</i>	1.8	$1475.3 \pm 3.8$	$1.51 \pm 0.09$	0.41	Rapid Rotation
WD J162157.79+043218.81	2025-05-29	McD/ProEM	1.76	10	<i>BG40</i>	1.4	$869.2 \pm 8.4$	$1.01 \pm 0.10$	0.46	Rapid Rotation
							$465.6 \pm 10.2$	$0.83 \pm 0.10$		
WD J184926.21+645810.98	2025-06-30	McD/ProEM	1.52	20	<i>BG40</i>	1.9	–	–	0.71	

**Table B2** *continued*

**Table B2** (*continued*)

Target	UT Date	Facility	Duration	$t_{\text{exp}}$	Filter	Seeing	$f$	$A$	S.T.	Variability
			hr	s		arcsec	$\mu\text{Hz}$	%	%	
WD J192555.20–034626.55	2025-10-24	PTO/PRISM	1.91	20	<i>BG40</i>	2.8	–	–	0.32	
WD J215331.59–262855.53	2025-10-24	PTO/PRISM	1.52	20	<i>BG40</i>	3.5	–	–	0.66	
WD J230844.31+034719.66	2024-11-27	McD/ProEM	3.38	20	<i>BG40</i>	1.4	$154.6 \pm 4.6$	$0.50 \pm 0.06$	0.30	Rapid Rotation
WD J234921.84+090714.70	2025-09-17	PTO/PRISM	2.05	15	<i>BG40</i>	3.0	$271.3 \pm 6.7$	$0.35 \pm 0.06$	–	
							–	–	0.57	

NOTE—We derive average seeing estimates from the FWHM found at each image by `hipercam` during our extraction. The frequencies and amplitudes we report are obtained from LLS fits to the time series using `pyr1d`. For objects with multiple periodicities, we list them in order by amplitude. We estimate uncertainties on these parameters using the framework provided by [Montgomery & O'Donoghue \(1999\)](#). S.T. is our abbreviation for the 0.1% false-alarm probability significance thresholds we bootstrap.

### C. Q BRANCH SAMPLE

We present our full Q branch sample within 100 pc in Table C1, highlighting both the delayed subset and the young subset. We include the target names and Gaia source id, the publication source for the target spectrum, the distance (pc) reported in Bailer-Jones et al. (2018), the transverse velocity  $v_t$  as calculated from Equation 1. We report the bootstrapped NOV variability limits from our photometric follow-up as detailed in Table B2 when available. For the remaining targets, we report the bootstrapped NOV variability limits from ZTF for targets at declinations higher than 30 deg, or ATLAS for targets at declinations lower than 30 deg. Finally, we include the spectral type of each target. All corresponding uncertainties are included. The targets are ranked alphabetically in each subset.

Table C1. Full Q branch sample within 100 pc

Target	Gaia source id	Spec. source	Distance	$v_t$	Sig. Thresh	Spectral Type
Delayed Subset						
WD J004527.50-233629.29	2348747743931814656	This Work	47.4 (0.3)	71.3 (0.3)	0.91	DQ
WD J010413.65+465043.18	401215160231429120	Kilic et al. (2020)	83.8 (1.1)	50.3 (0.5)	0.2	DQ
WD J012709.06-575914.45	4909586088245414912	This Work	93.8 (0.9)	72.3 (0.5)	3.44	DA
WD J020549.70+205707.96	94276941624384000	Jewett et al. (2024)	85.4 (1.0)	133.1 (1.3)	0.63	DAQ
WD J034703.18-180253.49	5107322396824711680	Jewett et al. (2024)	76.4 (0.8)	58.9 (0.5)	1.35	DA
WD J040104.29+214025.06	53042472446551424	Jewett et al. (2024)	71.4 (0.6)	88.4 (0.5)	0.5	DA
WD J044747.69+422438.69	203678825329613312	Jewett et al. (2024)	95.7 (1.6)	88.5 (1.0)	1.78	DA
WD J045533.97-005815.35	3226519762223501696	This Work	91.7 (1.3)	91.9 (1.0)	3.48	DA
WD J05274.33-310655.56	2905067333001582720	Subasavage et al. (2007)	40.9 (0.1)	69.2 (0.1)	1.21	DA
WD J052950.55+523953.39	263082591016645504	Gianninas et al. (2011)	38.9 (0.1)	122.1 (0.2)	0.2	DA
WD J065535.59+293909.66	887758130788405504	Jewett et al. (2024)	79.4 (0.7)	71.9 (0.5)	0.41	DAQ
WD J080122.81+774957.21	1138353770109251200	This Work	79.4 (0.6)	55.2 (0.3)	0.4	DA
WD J083135.57-223133.63	5702793425999272576	Kilic et al. (2020)	82.0 (0.9)	99.1 (0.7)		DAQ
WD J110703.79+040543.60	3815200997858084480	Kilic et al. (2020)	62.4 (0.5)	68.7 (0.4)	1.58	DA
WD J120331.90+645101.41	1585063422960992256	SDSS	87.1 (0.8)	63.3 (0.5)	0.5	DQA
WD J134347.63-442902.53	6108445596683010688	This Work	97.8 (2.4)	112.7 (1.5)	12.97	DQA
WD J151949.65+632951.86	1643814211883928320	Gianninas et al. (2011)	55.7 (0.2)	61.7 (0.1)	0.23	DA
WD J161556.15-395346.09	5994123531590244480	This Work	75.3 (0.7)	77.9 (0.6)	3.46	DA
WD J162236.25+300455.29	1318204460477280512	SDSS	74.7 (0.5)	53.1 (0.3)	0.25	DQA
WD J165915.38+661032.66	163568779016307976	Gianninas et al. (2011)	64.5 (0.3)	59.2 (0.2)		DA
WD J170145.15-524609.22	593593315435083872	This Work	40.5 (0.1)	59.7 (0.1)	3.96	DAQ
WD J170618.72-083747.26	4336571785203401472	Jewett et al. (2024)	67.7 (0.8)	136.7 (1.0)	0.76	DQA
WD J171034.72-200541.95	4128167950420485632	Jewett et al. (2024)	87.3 (1.8)	52.6 (0.6)	0.91	DQA
WD J172856.22+555822.63	1422012892308493568	SDSS	47.1 (0.1)	56.3 (0.1)	0.18	DQA
WD J183302.73-412058.38	6723335899591792512	This Work	74.8 (0.6)	58.2 (0.4)	3.78	DA
WD J184809.11-461958.62	670552153700215936	This Work	93.9 (1.3)	98.4 (1.0)	5.92	DA
WD J192407.28-271750.43	6765861019327924736	Jewett et al. (2024)	70.7 (0.8)	84.3 (0.7)	0.54	DA
WD J201115.28+491037.78	2087569060381096960	Jewett et al. (2024)	73.6 (0.5)	58.0 (0.3)	0.34	DQ
WD J214023.96-363757.44	6589369272547881856	Subasavage et al. (2007)	39.7 (0.2)	55.5 (0.1)	1.62	DQ
WD J234043.98-181945.62	2393834386459511680	Kilic et al. (2020)	96.1 (2.1)	51.1 (0.7)		DAQ

Table C1 *continued*

Table C1 (*continued*)

Target	Gaia source id	Spec. source	Distance	$v_t$	Sig. Thresh	Spectral Type
		pc	km s <sup>-1</sup>	%	%	
<b>Young Subset</b>						
WD J001534.13-604927.14	4904968208127215104	This Work	73.9 (0.6)	37.9 (0.2)	3.61	DH
WD J002959.00+364834.86	366784816895496064	Kilic et al. (2020)	59.5 (0.6)	28.4 (0.1)	DA	DA
WD J010745.24+290420.82	308383019835259008	Kilic et al. (2020)	59.1 (0.4)	14.1 (0.1)	0.19	DA
WD J013517.57+572249.29	412839403319209600	Kilic et al. (2020)	51.0 (0.2)	29.1 (0.1)	DA	DA
WD J025001.75-043703.17	5184589747536175104	SDSS	91.3 (1.5)	10.7 (0.1)	0.52	DH
WD J032547.53-081549.36	5168129306849447552	Jewett et al. (2024)	86.5 (1.2)	11.5 (0.1)	0.84	DA
WD J042226.08-240724.12	4896474240286811648	Jewett et al. (2024)	71.6 (0.4)	29.4 (0.1)	1.9	DA
WD J045919.46-540320.77	4782830054172758272	This Work	92.2 (1.0)	38.6 (0.3)	3.08	DA
WD J050709.66-264515.13	3421894079307215744	Guo et al. (2015)	53.8 (0.2)	11.7 (0.0)	0.42	DAH
WD J055134.45+413529.95	192275966334956672	Kilic et al. (2020)	46.4 (0.2)	29.8 (0.1)	DAQ	DAQ
WD J062335.30+190244.00	3372355922219793536	Jewett et al. (2024)	94.9 (1.6)	17.7 (0.3)	DH	DH
WD J065711.00+734144.97	1114813977776610944	Jewett et al. (2024)	82.9 (1.0)	15.2 (0.1)	0.67	DA
WD J072026.97-413924.27	55606337430205458304	This Work	97.3 (1.3)	32.3 (0.3)	10.68	DH
WD J073744.49-061018.89	305599768051212416	Jewett et al. (2024)	77.4 (0.9)	12.6 (0.1)	0.55	DQ
WD J081149.35+421208.95	921804126089222784	Gianninas et al. (2011)	91.8 (1.2)	36.1 (0.4)	0.55	DA
WD J094500.96-685304.67	5243591401210032000	This Work	85.5 (0.9)	16.7 (0.1)	3.81	DQ
WD J094928.05-514958.10	5405554510567061120	This Work	91.5 (1.0)	28.7 (0.2)	8.51	DA
WD J095057.58-284115.39	5464929134894103808	Jewett et al. (2024)	78.8 (0.7)	12.9 (0.1)	1.33	DA
WD J095328.98-671447.92	5245657246123148672	This Work	92.7 (1.2)	17.5 (0.2)	4.7	DH
WD J100219.81-371352.08	5422144977092449632	This Work	43.2 (0.1)	26.4 (0.0)	2.15	DH
WD J110732.92-160705.38	3559496413333223936	SDSS	83.9 (1.3)	48.8 (0.5)	2.33	DA
WD J113502.24-243020.09	3533885454629567872	Jewett et al. (2024)	75.7 (0.9)	41.2 (0.3)	2.1	DA
WD J115618.17-675029.94	523563774642886272	This Work	90.7 (1.0)	43.8 (0.3)	DA	DA
WD J133340.35+640627.35	1665858350572796672	SDSS	100.0 (1.4)	31.9 (0.3)	0.63	DAH
WD J145902.72-041157.75	6338900661178928896	Jewett et al. (2024)	60.7 (0.6)	22.9 (0.1)	DH	DH
WD J162157.79+043218.81	4436905352274528896	Kilic et al. (2020)	61.3 (0.3)	19.7 (0.1)	DH	DH
WD J162659.59+253326.79	1304081783374935680	Kilic et al. (2020)	83.9 (0.7)	23.8 (0.1)	DA	DA
WD J175253.90-663452.57	5812676526434412928	This Work	53.8 (0.2)	45.9 (0.1)	3.17	DQ
WD J175931.34-620108.87	5911160263973498496	O'Brien et al. (2023)	38.3 (0.1)	20.0 (0.0)	3.88	DA
WD J183449.52-450730.01	6709422675147738752	This Work	89.0 (1.3)	12.0 (0.1)	5.5	DA
WD J184926.21+645810.98	2253826832091026560	Kilic et al. (2020)	86.4 (0.7)	12.9 (0.1)	0.32	DH
WD J192555.20-034626.55	4213471120498390784	Jewett et al. (2024)	56.8 (0.3)	27.2 (0.1)	0.34	DQA
WD J193431.84-653025.80	6440255975194724736	This Work	96.9 (1.6)	43.9 (0.5)	4.41	DQA

Table C1 *continued*

Table C1 (*continued*)

Target	Gaia source id	Spec. source	Distance pc	$v_t$ km s <sup>-1</sup>	Sig. Thresh %	Spectral Type
WD J194736.29-310038.84	6751474223204472576	This Work	72.4 (0.9)	23.6 (0.2)	1.92	DAH
WD J204453.39-432919.16	6676948033760503296	This Work	49.9 (0.2)	14.2 (0.0)	1.7	DA
WD J205208.50-501335.57	6477825157941375232	This Work	100.0 (1.6)	36.7 (0.5)	4.7	DH
WD J205442.80-203925.93	6857295585945072128	Gianninas et al. (2011)	31.2 (0.0)	10.3 (0.0)	0.33	DA
WD J210547.70+590311.34	2190645256129430144	Jewett et al. (2024)	95.7 (1.0)	26.4 (0.2)	0.53	DA
WD J212401.83-6000059.54	6452369226077816064	This Work	90.4 (1.5)	44.6 (0.4)	5.83	DA
WD J215201.03-724022.50	6371070309824311808	This Work	92.2 (0.9)	12.7 (0.1)	3.92	DA
WD J215331.59-202855.53	6811977801160882944	Jewett et al. (2024)	79.2 (1.0)	16.3 (0.1)	0.73	DA
WD J222609.28-311141.35	6602096222717844224	Croom et al. (2004)	95.4 (1.4)	23.3 (0.3)	2.77	DA
WD J230658.73-290514.86	6606362529696816896	This Work	95.2 (1.9)	5.5 (0.1)	2.47	DA
WD J230844.31+034719.66	2662208372887759744	Kilic et al. (2020)	64.6 (0.6)	28.6 (0.2)	DQA	
WD J234921.84+090714.70	2758938385082121216	Kilic et al. (2020)	86.1 (1.1)	14.1 (0.1)	0.63	DA

NOTE—Distances and confidence interval of the estimated distance are reported from Bailer-Jones et al. (2018). Sig. Thresh is the abbreviation for the 0.1% false-alarm probability significance thresholds we bootstrap. The values for targets at declinations lower than 30 deg are from ATLAS. Otherwise, we pick the lower value between ZTF and our follow-up described in Table B2.

## REFERENCES

Althaus, L. G., Gil-Pons, P., Córscico, A. H., et al. 2021, *A&A*, 646, A30, doi: [10.1051/0004-6361/202038930](https://doi.org/10.1051/0004-6361/202038930)

Astropy Collaboration, Robitaille, T. P., Tollerud, E. J., et al. 2013, *A&A*, 558, A33, doi: [10.1051/0004-6361/201322068](https://doi.org/10.1051/0004-6361/201322068)

Astropy Collaboration, Price-Whelan, A. M., Sipőcz, B. M., et al. 2018, *AJ*, 156, 123, doi: [10.3847/1538-3881/aabc4f](https://doi.org/10.3847/1538-3881/aabc4f)

Astropy Collaboration, Price-Whelan, A. M., Lim, P. L., et al. 2022, *ApJ*, 935, 167, doi: [10.3847/1538-4357/ac7c74](https://doi.org/10.3847/1538-4357/ac7c74)

Bagnulo, S., & Landstreet, J. D. 2022, *ApJL*, 935, L12, doi: [10.3847/2041-8213/ac84d3](https://doi.org/10.3847/2041-8213/ac84d3)

Bailer-Jones, C. A. L., Rybizki, J., Fouesneau, M., Demleitner, M., & Andrae, R. 2021, *AJ*, 161, 147, doi: [10.3847/1538-3881/ab806](https://doi.org/10.3847/1538-3881/ab806)

Bailer-Jones, C. A. L., Rybizki, J., Fouesneau, M., Mantelet, G., & Andrae, R. 2018, *AJ*, 156, 58, doi: [10.3847/1538-3881/aacb21](https://doi.org/10.3847/1538-3881/aacb21)

Ballantyne, H. A., Espaas, T., Norgrove, B. Z., et al. 2021, *MNRAS*, 507, 4507, doi: [10.1093/mnras/stab2324](https://doi.org/10.1093/mnras/stab2324)

Barrientos, M., Kilic, M., Blouin, S., et al. 2025, *ApJL*, 990, L47, doi: [10.3847/2041-8213/adfc4a](https://doi.org/10.3847/2041-8213/adfc4a)

Bauer, E. B., Dotter, A., Conroy, C., et al. 2025, arXiv e-prints, arXiv:2509.21717, doi: [10.48550/arXiv.2509.21717](https://doi.org/10.48550/arXiv.2509.21717)

Bauer, E. B., Schwab, J., Bildsten, L., & Cheng, S. 2020, *ApJ*, 902, 93, doi: [10.3847/1538-4357/abb5a5](https://doi.org/10.3847/1538-4357/abb5a5)

Bédard, A., Blouin, S., & Cheng, S. 2024, *Nature*, 627, 286, doi: [10.1038/s41586-024-07102-y](https://doi.org/10.1038/s41586-024-07102-y)

Bell, K. 2022, Pyriod: Period detection and fitting routines, Astrophysics Source Code Library, record ascl:2207.007. <http://ascl.net/2207.007>

Berdyugin, A. V., Piironen, V., Bagnulo, S., Landstreet, J. D., & Berdyugina, S. V. 2023, *A&A*, 670, A2, doi: [10.1051/0004-6361/202245149](https://doi.org/10.1051/0004-6361/202245149)

Bhattacharya, M., Hackett, A. J., Gupta, A., Tout, C. A., & Mukhopadhyay, B. 2022, *ApJ*, 925, 133, doi: [10.3847/1538-4357/ac450b](https://doi.org/10.3847/1538-4357/ac450b)

Bida, T. A., Dunham, E. W., Massey, P., & Roe, H. G. 2014, in Society of Photo-Optical Instrumentation Engineers (SPIE) Conference Series, Vol. 9147, Ground-based and Airborne Instrumentation for Astronomy V, ed. S. K. Ramsay, I. S. McLean, & H. Takami, 91472N, doi: [10.1117/12.2056872](https://doi.org/10.1117/12.2056872)

Blouin, S., Daligault, J., & Saumon, D. 2021, *ApJL*, 911, L5, doi: [10.3847/2041-8213/abf14b](https://doi.org/10.3847/2041-8213/abf14b)

Blouin, S., Daligault, J., Saumon, D., Bédard, A., & Brassard, P. 2020a, *A&A*, 640, L11, doi: [10.1051/0004-6361/202038879](https://doi.org/10.1051/0004-6361/202038879)

Blouin, S., Kilic, M., Bédard, A., & Tremblay, P.-E. 2023, *MNRAS*, 525, L112, doi: [10.1093/mnrasl/slad105](https://doi.org/10.1093/mnrasl/slad105)

Blouin, S., Shaffer, N. R., Saumon, D., & Starrett, C. E. 2020b, *ApJ*, 899, 46, doi: [10.3847/1538-4357/ab9e75](https://doi.org/10.3847/1538-4357/ab9e75)

Brickhill, A. J. 1991, *MNRAS*, 251, 673, doi: [10.1093/mnras/251.4.673](https://doi.org/10.1093/mnras/251.4.673)

Briggs, G. P., Ferrario, L., Tout, C. A., Wickramasinghe, D. T., & Hurley, J. R. 2015, *MNRAS*, 447, 1713, doi: [10.1093/mnras/stu2539](https://doi.org/10.1093/mnras/stu2539)

Caiazzo, I., Burdge, K. B., Fuller, J., et al. 2021, *Nature*, 595, 39, doi: [10.1038/s41586-021-03615-y](https://doi.org/10.1038/s41586-021-03615-y)

Camisassa, M. E., Althaus, L. G., Torres, S., et al. 2021, *A&A*, 649, L7, doi: [10.1051/0004-6361/202140720](https://doi.org/10.1051/0004-6361/202140720)

Camisassa, M. E., Althaus, L. G., Córscico, A. H., et al. 2019, *A&A*, 625, A87, doi: [10.1051/0004-6361/201833822](https://doi.org/10.1051/0004-6361/201833822)

Caplan, M. E., Freeman, I. F., Horowitz, C. J., Cumming, A., & Bellinger, E. P. 2021, *ApJL*, 919, L12, doi: [10.3847/2041-8213/ac1f99](https://doi.org/10.3847/2041-8213/ac1f99)

Caplan, M. E., Horowitz, C. J., & Cumming, A. 2020, *ApJL*, 902, L44, doi: [10.3847/2041-8213/abbda0](https://doi.org/10.3847/2041-8213/abbda0)

Castro-Tapia, M., Zhang, S., & Cumming, A. 2024, *ApJ*, 975, 63, doi: [10.3847/1538-4357/ad7a6a](https://doi.org/10.3847/1538-4357/ad7a6a)

Cheng, S., Cummings, J. D., & Ménard, B. 2019, *ApJ*, 886, 100, doi: [10.3847/1538-4357/ab4989](https://doi.org/10.3847/1538-4357/ab4989)

Cheng, S., Cummings, J. D., Ménard, B., & Toonen, S. 2020, *ApJ*, 891, 160, doi: [10.3847/1538-4357/ab733c](https://doi.org/10.3847/1538-4357/ab733c)

Cheng, Y., & Takata, J. 2025, *MNRAS*, 539, 3013, doi: [10.1093/mnras/staf580](https://doi.org/10.1093/mnras/staf580)

Clemens, J. C., Crain, J. A., & Anderson, R. 2004, in Society of Photo-Optical Instrumentation Engineers (SPIE) Conference Series, Vol. 5492, Ground-based Instrumentation for Astronomy, ed. A. F. M. Moorwood & M. Iye, 331–340, doi: [10.1117/12.550069](https://doi.org/10.1117/12.550069)

Córscico, A. H., Althaus, L. G., Miller Bertolami, M. M., & Kepler, S. O. 2019, *A&A Rv*, 27, 7, doi: [10.1007/s00159-019-0118-4](https://doi.org/10.1007/s00159-019-0118-4)

Coutu, S., Dufour, P., Bergeron, P., et al. 2019, *ApJ*, 885, 74, doi: [10.3847/1538-4357/ab46b9](https://doi.org/10.3847/1538-4357/ab46b9)

Craig, M., Crawford, S., Seifert, M., et al. 2017, *astropy/ccdproc*: v1.3.0.post1, v1.3.0.post1, Zenodo, doi: [10.5281/zenodo.1069648](https://doi.org/10.5281/zenodo.1069648)

Croom, S. M., Smith, R. J., Boyle, B. J., et al. 2004, *MNRAS*, 349, 1397, doi: [10.1111/j.1365-2966.2004.07619.x](https://doi.org/10.1111/j.1365-2966.2004.07619.x)

Cunningham, T., Tremblay, P.-E., O'Brien, M., et al. 2025, *MNRAS*, 539, 2021, doi: [10.1093/mnras/staf428](https://doi.org/10.1093/mnras/staf428)

Dan, M., Rosswog, S., Brüggen, M., & Podsiadlowski, P. 2014, *MNRAS*, 438, 14, doi: [10.1093/mnras/stt1766](https://doi.org/10.1093/mnras/stt1766)

De Gerónimo, F. C., Uzundag, M., Rebassa-Mansergas, A., et al. 2025, *ApJL*, 980, L9, doi: [10.3847/2041-8213/adad73](https://doi.org/10.3847/2041-8213/adad73)

Dhillon, V. S., Bezawada, N., Black, M., et al. 2021, *MNRAS*, 507, 350, doi: [10.1093/mnras/stab2130](https://doi.org/10.1093/mnras/stab2130)

Dufour, P., Blouin, S., Coutu, S., et al. 2017, in *Astronomical Society of the Pacific Conference Series*, Vol. 509, 20th European White Dwarf Workshop, ed. P. E. Tremblay, B. Gaensicke, & T. Marsh, 3, doi: [10.48550/arXiv.1610.00986](https://doi.org/10.48550/arXiv.1610.00986)

Dufour, P., Vornanen, T., Bergeron, P., & Fontaine, A., B. 2013, in *Astronomical Society of the Pacific Conference Series*, Vol. 469, 18th European White Dwarf Workshop., ed. J. Krzesiński, G. Stachowski, P. Moskalik, & K. Bajan, 167

Dunlap, B. H., & Clemens, J. C. 2015, in *Astronomical Society of the Pacific Conference Series*, Vol. 493, 19th European Workshop on White Dwarfs, ed. P. Dufour, P. Bergeron, & G. Fontaine, 547

Ferrario, L., Vennes, S., Wickramasinghe, D. T., Bailey, J. A., & Christian, D. J. 1997, *MNRAS*, 292, 205, doi: [10.1093/mnras/292.2.205](https://doi.org/10.1093/mnras/292.2.205)

Fleury, L., Caiazzo, I., & Heyl, J. 2022, *MNRAS*, 511, 5984, doi: [10.1093/mnras/stac458](https://doi.org/10.1093/mnras/stac458)

—. 2023, *MNRAS*, 520, 364, doi: [10.1093/mnras/stad068](https://doi.org/10.1093/mnras/stad068)

Fontaine, G., Brassard, P., & Bergeron, P. 2001, *PASP*, 113, 409, doi: [10.1086/319535](https://doi.org/10.1086/319535)

Fontaine, G., Brassard, P., & Dufour, P. 2008, *A&A*, 483, L1, doi: [10.1051/0004-6361:200809651](https://doi.org/10.1051/0004-6361:200809651)

Fontaine, G., & Michaud, G. 1979, *ApJ*, 231, 826, doi: [10.1086/157247](https://doi.org/10.1086/157247)

Fontaine, G., Thomas, J. H., & van Horn, H. M. 1973, *ApJ*, 184, 911, doi: [10.1086/152381](https://doi.org/10.1086/152381)

Fuller, J., Piro, A. L., & Jermyn, A. S. 2019, *MNRAS*, 485, 3661, doi: [10.1093/mnras/stz514](https://doi.org/10.1093/mnras/stz514)

Gaia Collaboration, Babusiaux, C., van Leeuwen, F., et al. 2018, *A&A*, 616, A10, doi: [10.1051/0004-6361/201832843](https://doi.org/10.1051/0004-6361/201832843)

Gänsicke, B. T., Koester, D., Farihi, J., et al. 2012, *MNRAS*, 424, 333, doi: [10.1111/j.1365-2966.2012.21201.x](https://doi.org/10.1111/j.1365-2966.2012.21201.x)

García-Berro, E., Lorén-Aguilar, P., Aznar-Siguán, G., et al. 2012, *ApJ*, 749, 25, doi: [10.1088/0004-637X/749/1/25](https://doi.org/10.1088/0004-637X/749/1/25)

Gentile Fusillo, N. P., Tremblay, P.-E., Gänsicke, B. T., et al. 2019, *MNRAS*, 482, 4570, doi: [10.1093/mnras/sty3016](https://doi.org/10.1093/mnras/sty3016)

Gentile Fusillo, N. P., Tremblay, P. E., Cukanovaite, E., et al. 2021, *MNRAS*, 508, 3877, doi: [10.1093/mnras/stab2672](https://doi.org/10.1093/mnras/stab2672)

Gianninas, A., Bergeron, P., & Ruiz, M. T. 2011, *ApJ*, 743, 138, doi: [10.1088/0004-637X/743/2/138](https://doi.org/10.1088/0004-637X/743/2/138)

Ginsburg, A., Sipőcz, B. M., Brasseur, C. E., et al. 2019, *AJ*, 157, 98, doi: [10.3847/1538-3881/aafc33](https://doi.org/10.3847/1538-3881/aafc33)

Guidry, J. A., Vanderbosch, Z. P., Hermes, J. J., et al. 2021, *ApJ*, 912, 125, doi: [10.3847/1538-4357/abee68](https://doi.org/10.3847/1538-4357/abee68)

—. 2025, *ApJ*, 992, 167, doi: [10.3847/1538-4357/adfecb](https://doi.org/10.3847/1538-4357/adfecb)

Guo, J., Zhao, J., Tziampzis, A., et al. 2015, *MNRAS*, 454, 2787, doi: [10.1093/mnras/stv2104](https://doi.org/10.1093/mnras/stv2104)

Hallakoun, N., Maoz, D., Agol, E., et al. 2018, *MNRAS*, 476, 933, doi: [10.1093/mnras/sty257](https://doi.org/10.1093/mnras/sty257)

Harris, C. R., Millman, K. J., van der Walt, S. J., et al. 2020, *Nature*, 585, 357, doi: [10.1038/s41586-020-2649-2](https://doi.org/10.1038/s41586-020-2649-2)

Hermes, J. J., Kepler, S. O., Castanheira, B. G., et al. 2013, *ApJL*, 771, L2, doi: [10.1088/2041-8205/771/1/L2](https://doi.org/10.1088/2041-8205/771/1/L2)

Hermes, J. J., Gänsicke, B. T., Kawaler, S. D., et al. 2017, *ApJS*, 232, 23, doi: [10.3847/1538-4365/aa8bb5](https://doi.org/10.3847/1538-4365/aa8bb5)

Hernandez, M. S., Schreiber, M. R., Landstreet, J. D., et al. 2024, *MNRAS*, 528, 6056, doi: [10.1093/mnras/stae307](https://doi.org/10.1093/mnras/stae307)

Heyl, J. S., & Kulkarni, S. R. 1998, *ApJL*, 506, L61, doi: [10.1086/311628](https://doi.org/10.1086/311628)

Hollands, M. A., Tremblay, P. E., Gänsicke, B. T., et al. 2020, *Nature Astronomy*, 4, 663, doi: [10.1038/s41550-020-1028-0](https://doi.org/10.1038/s41550-020-1028-0)

Holmberg, J., Nordström, B., & Andersen, J. 2009, *A&A*, 501, 941, doi: [10.1051/0004-6361/200811191](https://doi.org/10.1051/0004-6361/200811191)

Hook, I. M., Jørgensen, I., Allington-Smith, J. R., et al. 2004, *PASP*, 116, 425, doi: [10.1086/383624](https://doi.org/10.1086/383624)

Hunter, J. D. 2007, *Computing in Science & Engineering*, 9, 90, doi: [10.1109/MCSE.2007.55](https://doi.org/10.1109/MCSE.2007.55)

Ingham, K., Gänsicke, B. T., Breedt, E., et al. 2023, *MNRAS*, 524, 4867, doi: [10.1093/mnras/stad2018](https://doi.org/10.1093/mnras/stad2018)

Janes, K. A., Clemens, D. P., Hayes-Gehrke, M. N., et al. 2004, in *American Astronomical Society Meeting Abstracts*, Vol. 204, American Astronomical Society Meeting Abstracts #204, 10.01

Jewett, G., Kilic, M., Bergeron, P., et al. 2024, *ApJ*, 974, 12, doi: [10.3847/1538-4357/ad6905](https://doi.org/10.3847/1538-4357/ad6905)

Jewett, G., Kilic, M., Moss, A., et al. 2025, arXiv e-prints, arXiv:2510.09802, doi: [10.48550/arXiv.2510.09802](https://doi.org/10.48550/arXiv.2510.09802)

Ji, S., Fisher, R. T., García-Berro, E., et al. 2013, *ApJ*, 773, 136, doi: [10.1088/0004-637X/773/2/136](https://doi.org/10.1088/0004-637X/773/2/136)

Kawka, A., Ferrario, L., & Vennes, S. 2023, *MNRAS*, 520, 6299, doi: [10.1093/mnras/stad553](https://doi.org/10.1093/mnras/stad553)

Kawka, A., Vennes, S., Schmidt, G. D., Wickramasinghe, D. T., & Koch, R. 2007, *ApJ*, 654, 499, doi: [10.1086/509072](https://doi.org/10.1086/509072)

Keller, S. C., Schmidt, B. P., Bessell, M. S., et al. 2007, *PASA*, 24, 1, doi: [10.1071/AS07001](https://doi.org/10.1071/AS07001)

Kilic, M., Bergeron, P., Blouin, S., et al. 2024, *ApJ*, 965, 159, doi: [10.3847/1538-4357/ad9bb3](https://doi.org/10.3847/1538-4357/ad9bb3)

—. 2025, *ApJ*, 979, 157, doi: [10.3847/1538-4357/ad9bb3](https://doi.org/10.3847/1538-4357/ad9bb3)

Kilic, M., Bergeron, P., Kosakowski, A., et al. 2020, *ApJ*, 898, 84, doi: [10.3847/1538-4357/ab9b8d](https://doi.org/10.3847/1538-4357/ab9b8d)

Kilic, M., Moss, A. G., Kosakowski, A., et al. 2023, *MNRAS*, 518, 2341, doi: [10.1093/mnras/stac3182](https://doi.org/10.1093/mnras/stac3182)

Kleinman, S. J., Kepler, S. O., Koester, D., et al. 2013, *ApJS*, 204, 5, doi: [10.1088/0067-0049/204/1/5](https://doi.org/10.1088/0067-0049/204/1/5)

Koester, D., Gänsicke, B. T., & Farihi, J. 2014, *A&A*, 566, A34, doi: [10.1051/0004-6361/201423691](https://doi.org/10.1051/0004-6361/201423691)

Koester, D., & Weidemann, V. 1982, *A&A*, 108, 406

Kurtz, D. W., Shibahashi, H., Dhillon, V. S., et al. 2013, *MNRAS*, 432, 1632, doi: [10.1093/mnras/stt585](https://doi.org/10.1093/mnras/stt585)

Lanza, A. F., Rui, N. Z., Farihi, J., Landstreet, J. D., & Bagnulo, S. 2024, *A&A*, 689, A233, doi: [10.1051/0004-6361/202449947](https://doi.org/10.1051/0004-6361/202449947)

Lauffer, G. R., Romero, A. D., & Kepler, S. O. 2018, *MNRAS*, 480, 1547, doi: [10.1093/mnras/sty1925](https://doi.org/10.1093/mnras/sty1925)

Lomb, N. R. 1976, *Ap&SS*, 39, 447, doi: [10.1007/BF00648343](https://doi.org/10.1007/BF00648343)

Maoz, D., Mazeh, T., & McQuillan, A. 2015, *MNRAS*, 447, 1749, doi: [10.1093/mnras/stu2577](https://doi.org/10.1093/mnras/stu2577)

Masci, F. J., Laher, R. R., Rusholme, B., et al. 2019, *PASP*, 131, 018003, doi: [10.1088/1538-3873/aae8ac](https://doi.org/10.1088/1538-3873/aae8ac)

Montgomery, M. H., & O'Donoghue, D. 1999, *Delta Scuti Star Newsletter*, 13, 28

Moss, A., Kilic, M., Bergeron, P., et al. 2025, *ApJ*, 990, 25, doi: [10.3847/1538-4357/aded8f](https://doi.org/10.3847/1538-4357/aded8f)

Muñoz, D. J., & Lai, D. 2015, *Proceedings of the National Academy of Science*, 112, 9264, doi: [10.1073/pnas.1505671112](https://doi.org/10.1073/pnas.1505671112)

Mukadam, A. S., Montgomery, M. H., Winget, D. E., Kepler, S. O., & Clemens, J. C. 2006, *ApJ*, 640, 956, doi: [10.1086/500289](https://doi.org/10.1086/500289)

Newville, M., Otten, R., Nelson, A., et al. 2025, *LMFIT: Non-Linear Least-Squares Minimization and Curve-Fitting for Python*, 1.3.4, Zenodo, doi: [10.5281/zenodo.16175987](https://doi.org/10.5281/zenodo.16175987)

O'Brien, M. W., Tremblay, P. E., Gentile Fusillo, N. P., et al. 2023, *MNRAS*, 518, 3055, doi: [10.1093/mnras/stac3303](https://doi.org/10.1093/mnras/stac3303)

O'Brien, M. W., Tremblay, P.-E., Klein, B. L., et al. 2024, *MNRAS*, 527, 8687, doi: [10.1093/mnras/stad3773](https://doi.org/10.1093/mnras/stad3773)

Ould Rouis, L. B., Hermes, J. J., Gänsicke, B. T., et al. 2024, *ApJ*, 976, 156, doi: [10.3847/1538-4357/ad86bb](https://doi.org/10.3847/1538-4357/ad86bb)

Pakmor, R., Pelisoli, I., Justham, S., et al. 2024, *A&A*, 691, A179, doi: [10.1051/0004-6361/202451352](https://doi.org/10.1051/0004-6361/202451352)

pandas development team, T. 2024, *pandas-dev/pandas: Pandas*, v2.2.3, Zenodo, doi: [10.5281/zenodo.13819579](https://doi.org/10.5281/zenodo.13819579)

Pathak, P., Blouin, S., & Herwig, F. 2025, *ApJ*, 983, 158, doi: [10.3847/1538-4357/adc10f](https://doi.org/10.3847/1538-4357/adc10f)

Prochaska, J., Hennawi, J., Westfall, K., et al. 2020a, *The Journal of Open Source Software*, 5, 2308, doi: [10.21105/joss.02308](https://doi.org/10.21105/joss.02308)

Prochaska, J. X., Hennawi, J., Cooke, R., et al. 2020b, *pypeit/PypeIt: Release 1.0.0, v1.0.0*, Zenodo, doi: [10.5281/zenodo.3743493](https://doi.org/10.5281/zenodo.3743493)

Reding, J. S., Hermes, J. J., Vanderbosch, Z., et al. 2020, *ApJ*, 894, 19, doi: [10.3847/1538-4357/ab8239](https://doi.org/10.3847/1538-4357/ab8239)

Ricker, G. R., Winn, J. N., Vanderspek, R., et al. 2015, *Journal of Astronomical Telescopes, Instruments, and Systems*, 1, 014003, doi: [10.1117/1.JATIS.1.1.014003](https://doi.org/10.1117/1.JATIS.1.1.014003)

Romero, A. D., Antunes Amaral, L., Kepler, S. O., et al. 2020, *MNRAS*, 497, L24, doi: [10.1093/mnrasl/slaa106](https://doi.org/10.1093/mnrasl/slaa106)

Rui, N. Z., & Fuller, J. 2025, *arXiv e-prints*, arXiv:2601.00072, doi: [10.48550/arXiv.2601.00072](https://doi.org/10.48550/arXiv.2601.00072)

Rui, N. Z., Ong, J. M. J., & Mathis, S. 2024, *MNRAS*, 527, 6346, doi: [10.1093/mnras/stad3461](https://doi.org/10.1093/mnras/stad3461)

Sahu, S., Bédard, A., Gänsicke, B. T., et al. 2025, *Nature Astronomy*, 9, 1347, doi: [10.1038/s41550-025-02590-y](https://doi.org/10.1038/s41550-025-02590-y)

Scargle, J. D. 1982, *ApJ*, 263, 835, doi: [10.1086/160554](https://doi.org/10.1086/160554)

Schimczek, C., & Wunner, G. 2014, *ApJS*, 212, 26, doi: [10.1088/0067-0049/212/2/26](https://doi.org/10.1088/0067-0049/212/2/26)

Schwab, J. 2021, *ApJ*, 906, 53, doi: [10.3847/1538-4357/abc87e](https://doi.org/10.3847/1538-4357/abc87e)

Shen, K. J., Bildsten, L., Kasen, D., & Quataert, E. 2012, *ApJ*, 748, 35, doi: [10.1088/0004-637X/748/1/35](https://doi.org/10.1088/0004-637X/748/1/35)

Shen, K. J., Blouin, S., & Breivik, K. 2023, *ApJL*, 955, L33, doi: [10.3847/2041-8213/acf57b](https://doi.org/10.3847/2041-8213/acf57b)

Shibahashi, H. 2007, in *American Institute of Physics Conference Series*, Vol. 948, *Unsolved Problems in Stellar Physics: A Conference in Honor of Douglas Gough*, ed. R. J. Stencliffe, G. Houdek, R. G. Martin, & C. A. Tout (AIP), 35–42, doi: [10.1063/1.2818994](https://doi.org/10.1063/1.2818994)

Siess, L. 2007, *A&A*, 476, 893, doi: [10.1051/0004-6361:20078132](https://doi.org/10.1051/0004-6361:20078132)

Silvestri, N. M., Lemagie, M. P., Hawley, S. L., et al. 2007, *AJ*, 134, 741, doi: [10.1086/519242](https://doi.org/10.1086/519242)

Sion, E. M., Greenstein, J. L., Landstreet, J. D., et al. 1983, *ApJ*, 269, 253, doi: [10.1086/161036](https://doi.org/10.1086/161036)

Steen, M., Hermes, J. J., Gudrid, J. A., et al. 2024, *ApJ*, 967, 166, doi: [10.3847/1538-4357/ad3e60](https://doi.org/10.3847/1538-4357/ad3e60)

Subasavage, J. P., Henry, T. J., Bergeron, P., et al. 2007, *AJ*, 134, 252, doi: [10.1086/518739](https://doi.org/10.1086/518739)

Taylor, M. 2011, *TOPCAT: Tool for OPerations on Catalogues And Tables*, *Astrophysics Source Code Library*, record ascl:1101.010. <http://ascl.net/1101.010>

Temmink, K. D., Toonen, S., Zapartas, E., Justham, S., & Gänsicke, B. T. 2020, *A&A*, 636, A31, doi: [10.1051/0004-6361/201936889](https://doi.org/10.1051/0004-6361/201936889)

Tonry, J. L., Denneau, L., Heinze, A. N., et al. 2018, PASP, 130, 064505, doi: [10.1088/1538-3873/aabadf](https://doi.org/10.1088/1538-3873/aabadf)

Toonen, S., Nelemans, G., & Portegies Zwart, S. 2012, A&A, 546, A70, doi: [10.1051/0004-6361/201218966](https://doi.org/10.1051/0004-6361/201218966)

Tremblay, P.-E., Fontaine, G., Gentile Fusillo, N. P., et al. 2019, Nature, 565, 202, doi: [10.1038/s41586-018-0791-x](https://doi.org/10.1038/s41586-018-0791-x)

Uzundag, M., Kilic, M., De Gerónimo, F. C., et al. 2025, arXiv e-prints, arXiv:2511.06478.  
<https://arxiv.org/abs/2511.06478>

Van Grootel, V., Fontaine, G., Brassard, P., & Dupret, M.-A. 2015, A&A, 575, A125, doi: [10.1051/0004-6361/201425386](https://doi.org/10.1051/0004-6361/201425386)

Vanderbosch, Z. 2023, *zvanderbosch/phot2lc: phot2lc v1.7.8 release, v1.7.8*, Zenodo, doi: [10.5281/zenodo.8169807](https://doi.org/10.5281/zenodo.8169807)

VanderPlas, J. T. 2018, ApJS, 236, 16, doi: [10.3847/1538-4365/aab766](https://doi.org/10.3847/1538-4365/aab766)

Veras, D., & Tout, C. A. 2012, MNRAS, 422, 1648, doi: [10.1111/j.1365-2966.2012.20741.x](https://doi.org/10.1111/j.1365-2966.2012.20741.x)

Veras, D., Xu, S., & Rebassa-Mansergas, A. 2018, MNRAS, 473, 2871, doi: [10.1093/mnras/stx2141](https://doi.org/10.1093/mnras/stx2141)

Vincent, O., Bergeron, P., & Lafrenière, D. 2020, AJ, 160, 252, doi: [10.3847/1538-3881/abbe20](https://doi.org/10.3847/1538-3881/abbe20)

Virtanen, P., Gommers, R., Oliphant, T. E., et al. 2020, Nature Methods, 17, 261, doi: [10.1038/s41592-019-0686-2](https://doi.org/10.1038/s41592-019-0686-2)

Wegg, C., & Phinney, E. S. 2012, MNRAS, 426, 427, doi: [10.1111/j.1365-2966.2012.21394.x](https://doi.org/10.1111/j.1365-2966.2012.21394.x)

Wendell, C. E., van Horn, H. M., & Sargent, D. 1987, ApJ, 313, 284, doi: [10.1086/164968](https://doi.org/10.1086/164968)

Wes McKinney. 2010, in Proceedings of the 9th Python in Science Conference, ed. Stéfan van der Walt & Jarrod Millman, 56 – 61, doi: [10.25080/Majora-92bf1922-00a](https://doi.org/10.25080/Majora-92bf1922-00a)

Wickramasinghe, D. T., & Ferrario, L. 2000, PASP, 112, 873, doi: [10.1086/316593](https://doi.org/10.1086/316593)

Williams, K., Martinez, Z., & Ornelas, M. 2025, arXiv e-prints, arXiv:2510.18044, doi: [10.48550/arXiv.2510.18044](https://doi.org/10.48550/arXiv.2510.18044)

Williams, K. A., Montgomery, M. H., Winget, D. E., Falcon, R. E., & Bierwagen, M. 2016, ApJ, 817, 27, doi: [10.3847/0004-637X/817/1/27](https://doi.org/10.3847/0004-637X/817/1/27)

Wu, C., Xiong, H., & Wang, X. 2022, MNRAS, 512, 2972, doi: [10.1093/mnras/stac273](https://doi.org/10.1093/mnras/stac273)

Wu, Y., & Goldreich, P. 1999, ApJ, 519, 783, doi: [10.1086/307412](https://doi.org/10.1086/307412)

Xing, Z., Torres, S., Götberg, Y., et al. 2025, MNRAS, 537, 285, doi: [10.1093/mnras/stae2820](https://doi.org/10.1093/mnras/stae2820)

Yoon, S. C., Podsiadlowski, P., & Rosswog, S. 2007, MNRAS, 380, 933, doi: [10.1111/j.1365-2966.2007.12161.x](https://doi.org/10.1111/j.1365-2966.2007.12161.x)

Zuckerman, B., Koester, D., Reid, I. N., & Hünsch, M. 2003, ApJ, 596, 477, doi: [10.1086/377492](https://doi.org/10.1086/377492)